~~CONFIDENTIAL~~

Department of the Navy
Bureau of Ordnance
Contract NOrd 9612

A MODEL STUDY OF THE EFFECT OF JET AND EXHAUST FLOW ON DRAG OF THE TORPEDO TEST VEHICLE MK 40 X-1

R. L. Waid

Hydrodynamics Laboratory
California Institute of Technology
Pasadena, California

Report No. E-12.16
April, 1954

John T. McGraw
Project Supervisor

Copy No. 51

~~CONFIDENTIAL~~

CONTENTS

TABLE OF ILLUSTRATIONS

TABLE OF ILLUSTRATIONS (continued)

ABSTRACT

Experimental investigations of the effects of jets and exhaust on a model of the TTV Mk 40 X-1 are discussed. Photographs of the model jet and exhaust flow patterns are presented. Model pressure distribution data and afterbody drag coefficients are shown for numerous flow conditions. Many correlations among the observed phenomena are discussed. Several estimates of prototype jet- and exhaust-induced drag forces are presented. The susceptibility of the configuration to cavitation is discussed. Detailed analyses of the model results as they pertain to the prototype external flow phenomena are presented. Possible fields of study are suggested which could lead to improved prototype performance characteristics.

INTRODUCTION

The project reported herein is a continuation of specialized model studies which have augmented the full-scale research and development of the Torpedo Test Vehicle Mk 40 X-1. These model studies have been required to help explain some of the phenomena which have been observed during full-scale testing. Analysis of full-scale, high-speed runs provides only limited information about the many external hydrodynamic phenomena. Laboratory tests under controlled and stable conditions have been relied upon[1, 2*] to indicate the salient features of the complex external hydrodynamics.

Analysis of full-scale test data[1, 2] has shown a drag force which is considerably larger than the drag force of the unpropelled vehicle. The hydrodynamic difference between the unpropelled and the propelled configurations is the addition of eight water and exhaust jets. Calculations based on experimental model studies have shown that the presence of the water jets alone can cause sizable increases in the drag force.[3] These tests considered only the water jets, neglecting the exhaust gases and the exhaust ports. Model studies by this Laboratory[4] have verified the fact that jet flow exists over the entire length of the afterbody. Also, it was found that the water jets impinged upon the rear surface of the simulated exhaust ports. Several jet variations were mentioned which would eliminate the impingement and alleviate the high velocity shear flow over the afterbody. As in other model studies, this program did not investigate the effect of exhaust gas flow.

The present project was undertaken to investigate the external hydrodynamics of the TTV Mk 40 X-1 for simulated full-scale jet and exhaust flow ratios. Three separate phases of testing were undertaken. The first phase of the project consisted of a qualitative analysis of the model jet and exhaust flow patterns as recorded by time and flash photographs. These photographs are particularly useful when correlating the various effects observed during the subsequent phases of the research. Some of the results of this phase of the project are shown in Appendix I.

---

*Superscripts refer to the bibliography on page 46.

The second phase of the project consisted of obtaining extensive pressure distribution measurements. A broad area over the afterbody was investigated with particular emphasis in the areas immediately behind the jet and exhaust ports. It is in these areas that the significant changes in pressure distribution occur. Form drag coefficients were obtained from this data for various jet and exhaust flow ratios. The coefficients were used in a later analysis to separate the various causes of change in the drag force. The pressure distributions were important, also, from the standpoint of cavitation resistance. Appendix II presents some of the pressure distribution data.

The third phase of the research consisted of measurements of drag on the model afterbody. Because of structural restrictions it was not possible to mount the entire body on the present balance system. A special internal drag balance was devised to measure the drag force on the afterbody alone. A correlation of this data and the form drag information provided a satisfactory resolution of the jet-and exhaust-induced drag forces. As noted before, the more significant changes in drag forces are apt to occur over the afterbody. Although the results of this study do not produce explicit information about the entire torpedo configuration, the study does show the sources and order of magnitude of the changes in the drag forces. A summary of this data is found in Appendix III.

A correlation of the data from the three phases of the research has resulted in a resolution of the forces involved and a general understanding of the causes of these forces. The following sections of this report describe the experimental program and present the results of the analysis as it relates to the external hydrodynamics of the TTV Mk 40 X-1.

EXPERIMENTAL INVESTIGATION

Models

Figure 1 shows the 2-in. diameter model of the TTV Mk 40 X-1 which was tested in the High Speed Water Tunnel. The high aspect ratio tail fins were patterned after those used on the hydrodynamic version[1] (basic Lyon's Form "A" configuration) of the TTV Mk 40 X-1. The nose section of the model was assembled as a unit with the supporting strut.

As shown in Fig. 2, the water from the nose intake was ducted through a channel in the supporting strut to a pump which was located outside the water tunnel. From the pump the water was ducted through another channel in the strut and was discharged from the seven jet nozzles. The simulated exhaust gases (air) were ducted through the strut and discharged from the seven exhaust ports. Since only seven jets and exhausts were utilized, changes in data caused by jet and exhaust flows were corrected to an equivalent eight jet configuration. The afterbody section started immediately aft of the exhaust port. This section was separate from the nose and the supporting strut. A duplicate tail cone without fins was used for studying bare body characteristics.

The pressure distribution version of the Mk 40 is shown in Fig. 3. Three pressure taps were installed in the nose section. Ten taps were placed along a generating curve of the afterbody. Although the photograph shows the taps aligned with the jet axis, the entire afterbody could be rotated to any desired position. Thus, an extensive afterbody pressure distribution survey could be obtained. Two other taps were later placed in the tail cone midway between two adjacent fins. One tap was behind the leading edge of the fins and the other was ahead of the trailing edge of the fins.

The model, which incorporates the afterbody drag balance, is schematically represented in Fig. 4. The afterbody shell was attached to the balance yoke by means of two thin brass diaphragms. The yoke was fastened to the nose section. Drag forces deflected the shell relative to the fixed yoke. A variable reluctance device was used to determine the relative deflection. The device was calibrated by measuring the output voltage as a function of an applied load. The diaphragms served to support the afterbody shell, as well as to provide a linear spring constant for the purpose of force measurement. A pressure tap was placed in the region between the nose section and the free-floating afterbody section. This was necessary for determining the effective upstream force on the afterbody caused by the ambient pressure distribution. The balance actually records the upstream force minus the drag force. If the propelling force is calculated, the actual drag force can be obtained.

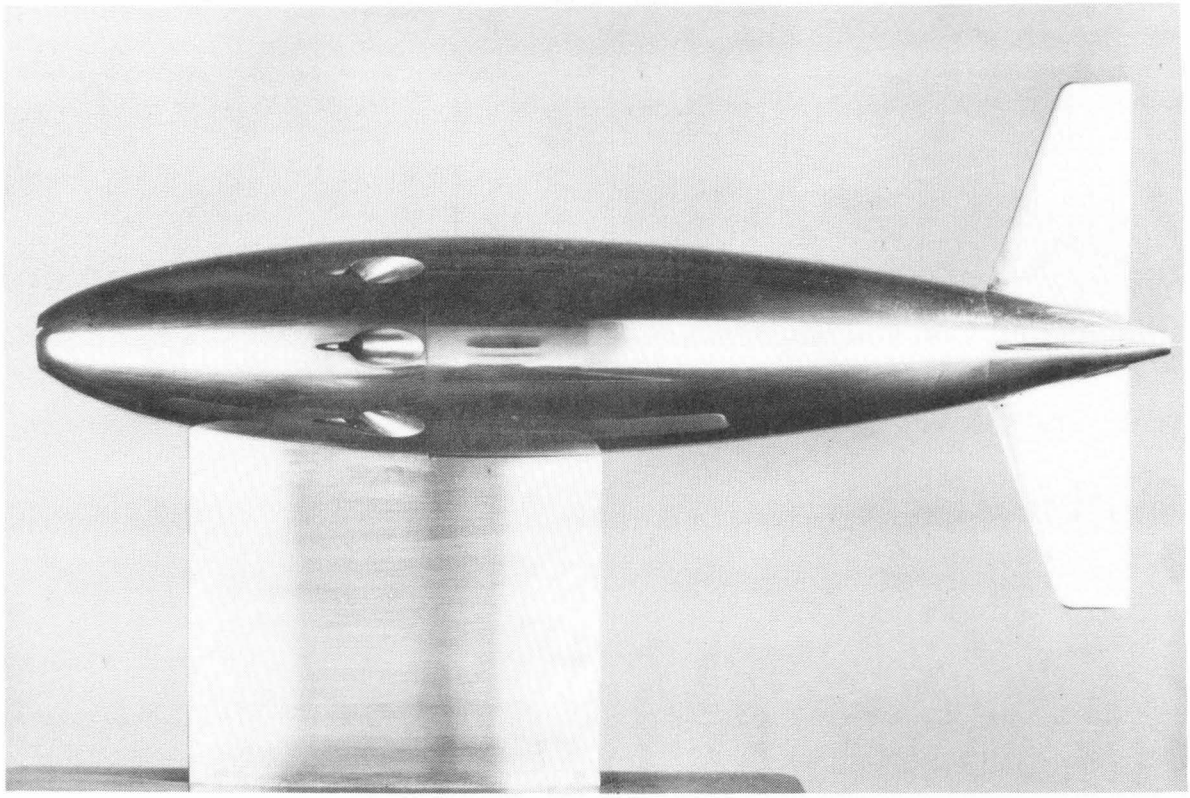

Fig. 1 - 2-in. diameter model of the torpedo test vehicle Mk 40 X-1.

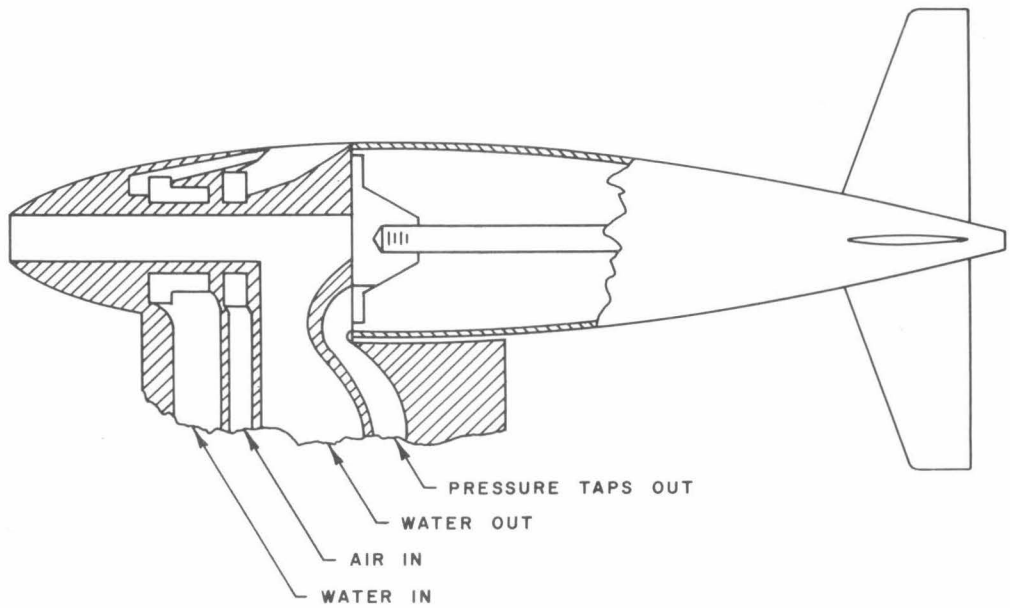

Fig. 2 - Internal arrangement of Model TTV Mk 40 X-1.

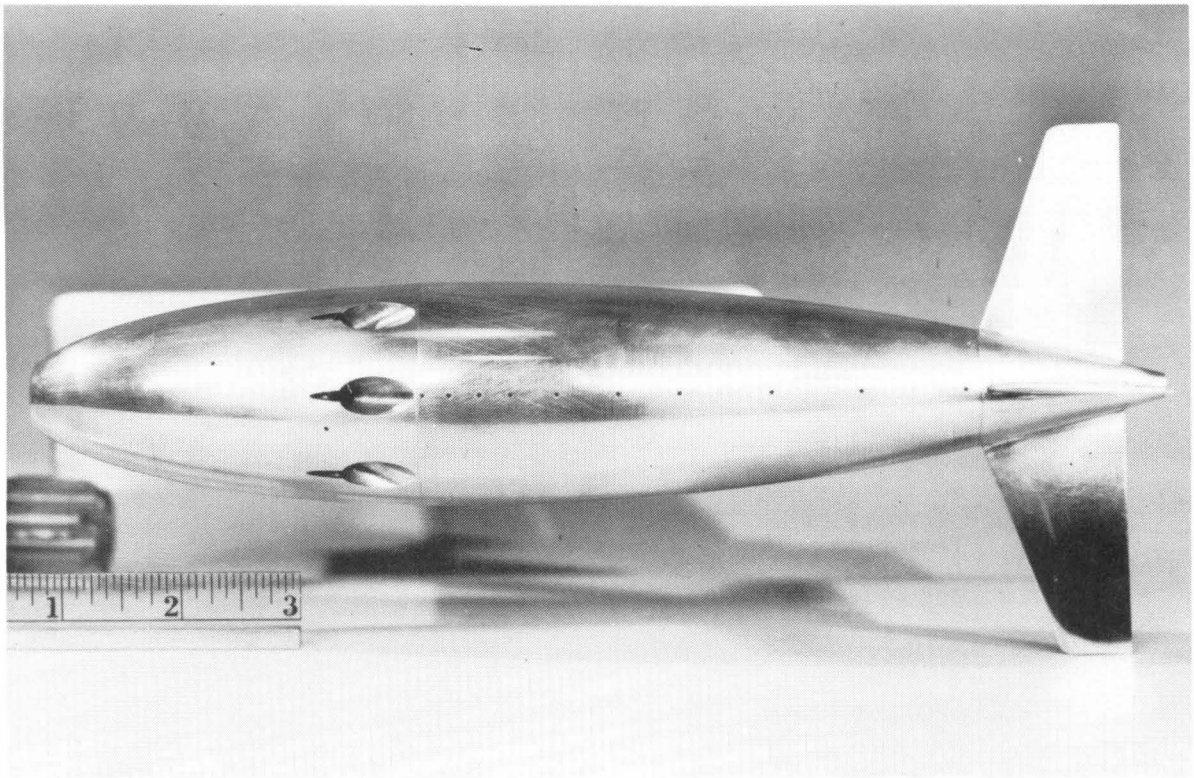

Fig. 3 - Pressure tap arrangement of Model TTV Mk 40 X-1.

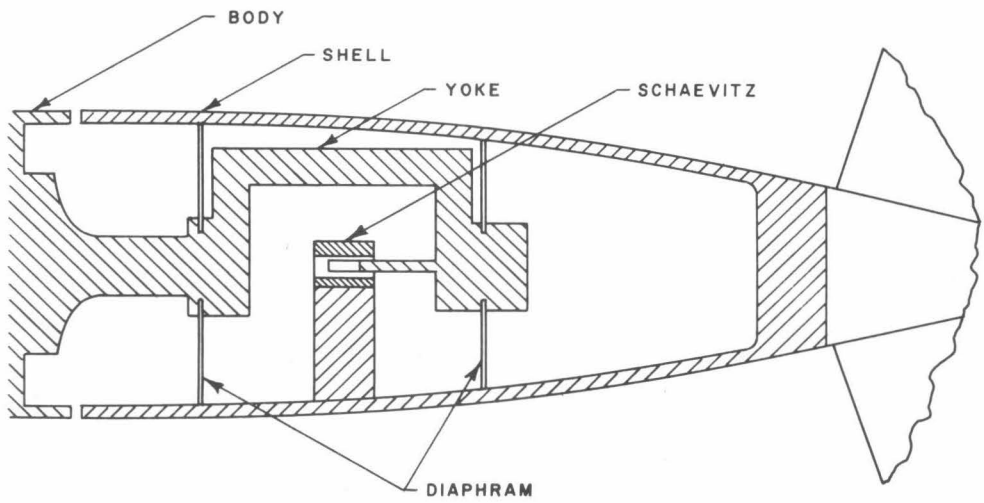

Fig. 4 - Schematic diagram of internal arrangement of model afterbody drag balance.

Special Equipment

The pressure distribution studies utilized a recently constructed 20-tube mercury manometer. The manometer board is back-lighted so that the data can be recorded instantaneously by photographs. Since there are no gas-liquid interface pots in the system, the manometer could not be utilized when high exhaust flow rates were studied.

The complete testing program was conducted in the High Speed Water Tunnel.

Test Program and Procedure

The qualitative studies were conducted photographically. To facilitate the analysis of the data, the model was painted with a white lacquer. The water jets were impregnated with a potassium permanganate dye solution. A light filter was used with the camera to increase the contrast between the dye and the white model. In general, the tests were conducted with a tunnel velocity of 30 fps. The jet-to-tunnel velocity ratio was varied from 0 to 2.7. The exhaust gas flow rate has been expressed as an exhaust "velocity". This "velocity" has been obtained by dividing the volume rate of discharge of the exhaust gas from the body by the area of the throat of the diverging exhaust nozzle. A range of exhaust-to-tunnel velocity ratios of 0 to 2 was tested. Prototype data which were supplied by the Naval Ordnance Test Station, China Lake, Foothill Annex, show operating exhaust flow rates which are equivalent to exhaust "velocity" ratios between 0.4 and 1.5. Figure 5 shows the prototype and model exhaust flow rates as a function of the exhaust "velocity" ratio. Time exposures (1/25 of a second) were taken for numerous combinations of flow ratios. Flash photographs (15 microseconds flash duration) were obtained at near operational flow ratios. Some of the results of this phase of the study are shown in Appendix I.

The pressure distribution tests were also conducted at a tunnel velocity of 30 fps. The jet-to-tunnel velocity ratio was varied from 0 to 2.7, as before. The simulated exhaust flow was tested at a jet-to-tunnel velocity ratio of 2.35. The exhaust-to-tunnel velocity ratios ranged from 0 to 1.0. The afterbody pressure taps were indexed over an angular range of 115° of the afterbody circumference. This included 2.5° increments in

the vicinity of the jet axes. The tail cone pressure taps were indexed over the same range as for the afterbody. All of these tests were conducted at a free-stream cavitation number of 5.8.

Afterbody drag force measurements of a simulated unpropelled configuration were obtained at tunnel velocities from 10 to 40 fps. The configurations tested included the bare body and the body with the high aspect ratio fins. The bare body was tested, also, at 20, 27, and 30 fps for various jet and exhaust velocity ratios. The jet-to-tunnel velocity ratio was varied from 0 to 2.7. For a jet ratio of 2.35 the exhaust velocity ratio was varied from 0 to 1.5. The finned body was tested at 20, 25, and 30 fps for similar jet and exhaust velocity ratios. The free stream pressure was 20 psig for all of these tests. A summary of this data is presented in Appendix III.

The fin-tailed model was tested with no jet flow for several exhaust velocity ratios up to 0.8. The results of this test are presented in Appendix IV.

RESULTS

Effects of the Forward Water Inlet

The placing of the water inlet at the stagnation point of the Lyon's Form "A"[5] shape alters the fluid flow pattern over the remainder of the body. Model pressure measurements show a definite difference in the pressure distribution. Figure 6 shows the effective model pressure distribution for the finless configuration. The effective pressure is the integrated average of the circumferential pressures. For this data the jet velocity ratio was 2.0 with no exhaust flow. The basic Lyon's Form "A" pressure distribution[5] is shown for comparison. A later section discusses the effect of jet flow on the pressure distribution. At this point it is sufficient to say that the jet flow has only a slight effect on the effective pressure distribution except in the region immediately aft of the exhaust port. The shape of the model Mk 40 pressure distribution is quite different than that of the Lyon's Form "A". The low pressure area of the Mk 40, excluding the pressure drop peak, is further towards the tail than for the Lyon's Form "A". This means that the form drag of the model Mk 40 is greater than for the Lyon's Form "A". The calculated afterbody form drag

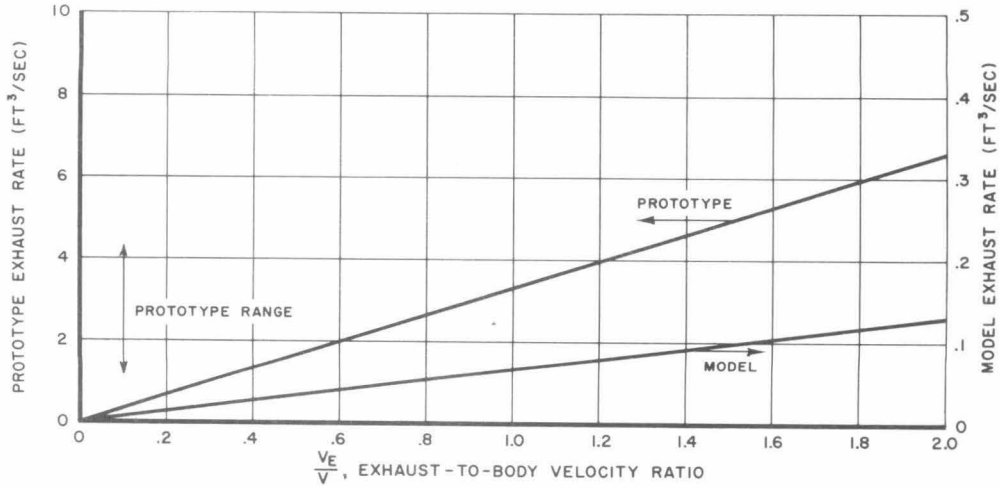

Fig. 5 - Prototype and model noncondensable exhaust flow rates versus the exhaust "velocity" ratio.

Prototype velocity 121 fps
Model velocity 30 fps
Prototype data from Run No. 48 (supplied by NOTS)

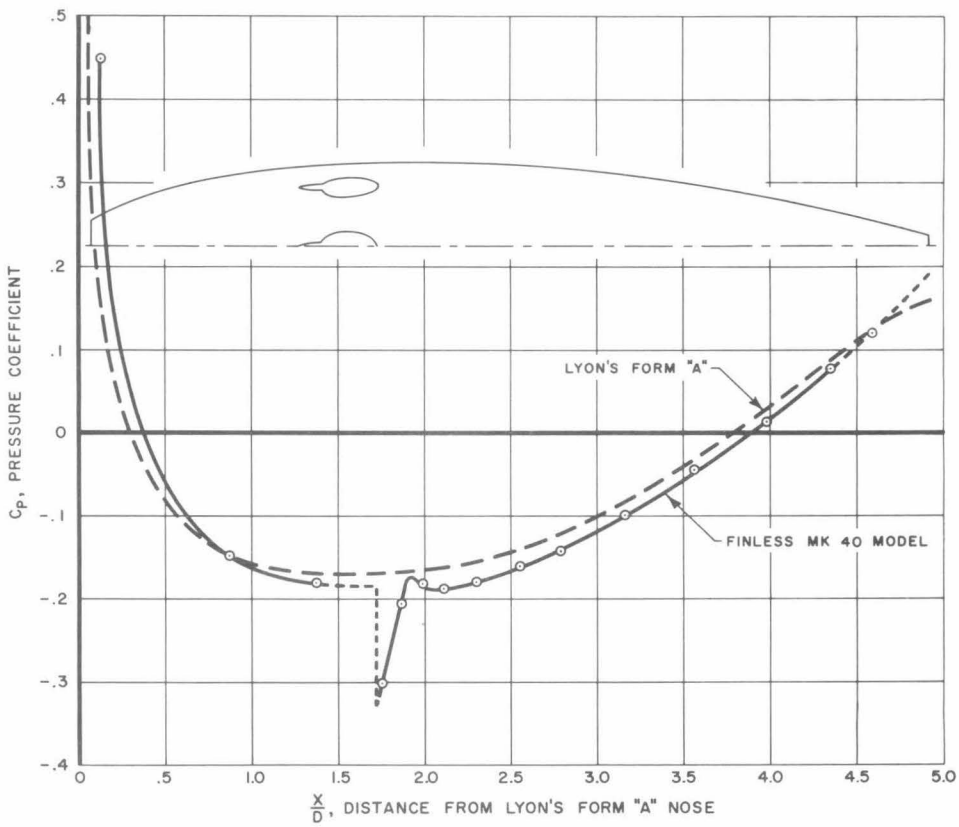

Fig. 6 - Effective pressure distribution on Model TTV Mk 40 X-1 for a jet-to-tunnel velocity ratio of 2.0. Lyon's Form "A" pressure distribution shown for comparison.

coefficient (based on cross section area) for the finless Mk 40 model is 0.0316 for a jet velocity ratio of 2.0, Table I.* The Lyon's Form "A" afterbody form drag coefficient is 0.0242. Thus, the form drag coefficient for the Mk 40 is 0.0074 greater than for the Lyon's Form "A". Whether this entire increase in form drag could be recovered by redesign is not known. The figures do show that the nose water inlet does affect the external hydrodynamics of the model afterbody.

The pressure distribution of the nose of the model Mk 40 indicates higher pressures than for the same position on the Lyon's Form "A". This causes the model Mk 40 nose form drag to be considerably higher than for the comparable Lyon's Form "A". Near the jet ports the Mk 40 pressure is lower than for the similar Lyon's Form "A". This causes a small reduction of the model Mk 40 nose form drag. Because of the unknown conditions in the water inlet, the following analysis considers only the components of the drag forces on the external surface of the nose. The calculated model Mk 40 nose form drag coefficient is -0.0276 as compared to -0.0726 for a similar portion of the Lyon's Form "A". The negative signs indicate a net propelling force on the external nose for this portion of the configuration. It should be pointed out that the above comparison of characteristics of the model Mk 40 configuration and the Lyon's Form "A" has been based solely on the fact that the body contours are identical with the exception of the nose duct area. Since there are no other available data on similar arrangements, there is no basis for a comparison other than that of similar shapes. Thus, this is not a rigorous comparison of the relative merits of the Mk 40 configuration. This analysis does emphasize the point that the optimum shape for a solid body is not necessarily the optimum shape for a nose ducted body.[6]

Because the above form drag comparisons are not rigorous, calculations of possible full scale drag force differences have not been made. Small modifications of the nose contour could improve the nose form drag. However, the quantitative effect of such a modification on the form drag of the nose or the afterbody cannot be anticipated. The purpose of this analysis is to point out the desirability of future studies of optimum nose ducted configurations for application to high performance weapons.

Effect of Fins on Afterbody Drag

Calculations, based on the pressure distributions, show an increase in the model afterbody form drag coefficient of 0.0025 by the addition of

*See page 33.

the high aspect-ratio fins. The experimentally determined change in the model afterbody form drag coefficient, from Fig. 7, is 0.0045. The latter increment includes the form drag of the fins as well as the form drag of the body. The scatter of the experimental data encompasses both values. The significance of this data is that the addition of the fins probably increases the prototype form drag about 125 lbs at a speed of 121 fps. This is approximately 4% of the total drag force,[1] Table II.* Other experimental data[3] indicate the addition of a shroud ring tail of the same surface area would increase the total drag force (friction and form) by 250 lbs.

Effect of Jet Impingement on Exhaust Port

Figure 8 shows the jet flow pattern for a jet-to-tunnel velocity ratio of 2.34 with no simulated exhaust flow. The actual pressure distribution, Fig. 9, along the axis of the jet shows a very sharp drop in the pressure coefficient in the local area immediately behind the exhaust port. A similar drop in pressure was reported previously[7] for a three-dimensional jet on a two-dimensional surface. The nozzle shape reported in Ref. 7 extended to the body surface. There was no simulated exhaust port. The magnitude of the model Mk 40 pressure peak for comparable conditions is much larger than that shown in Ref. 7. The shape and the position of the peak relative to the nozzle is also different. Hence, it can be assumed that the existence of the exhaust port causes these changes. The presence of the peak indicates that the jet does not flow parallel to the afterbody surface, but rather that it tends to separate more definitely from the surface than for the previously reported configuration. Since the jet angles are the same in both cases, it can be assumed that the jet of the Mk 40 is deflected from its intended path. To do this, the jet probably impinges upon the rear surface of the exhaust port. This occurrence has been predicted and analyzed in Ref. 4. Visual observation of the photographs, Fig. 8, shows the jet spraying in both radial and circumferential directions as the main part of the jet approaches the exhaust port. The spray indicates that the jet has impinged upon the port and has been deflected from its original path. The impingement and deflection of a sizable portion of the jet must result in a force in the drag direction. Thus, it appears that the model drag would be increased.

Estimation of full scale jet impingement drag (no exhaust flow

*See page 34.

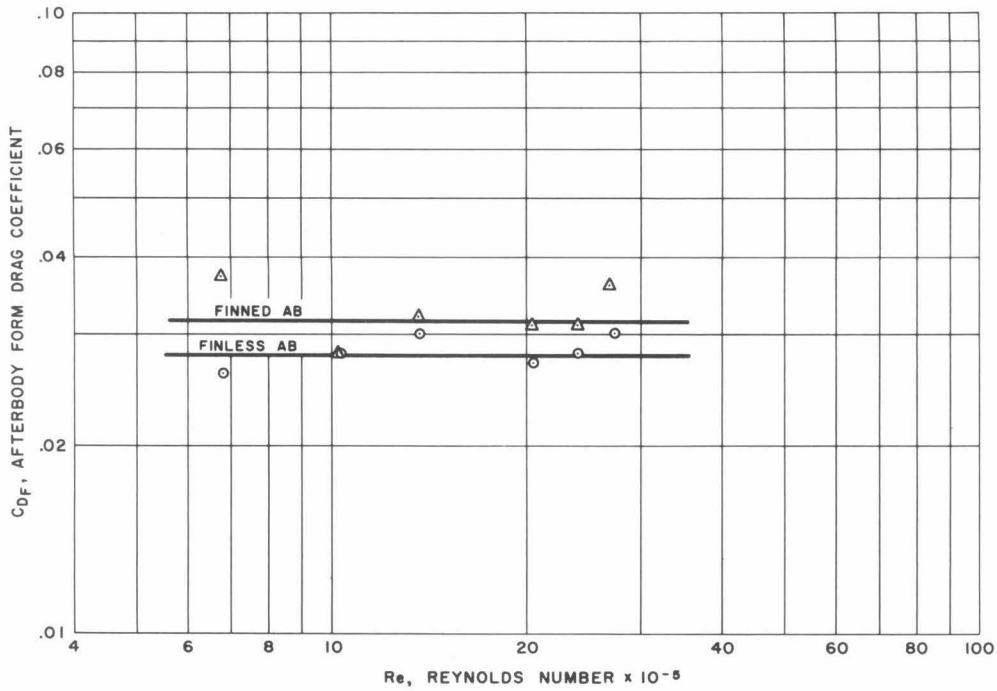

Fig. 7 - Afterbody form drag coefficients calculated from drag data versus Reynolds number. **No jet or exhaust flow.**

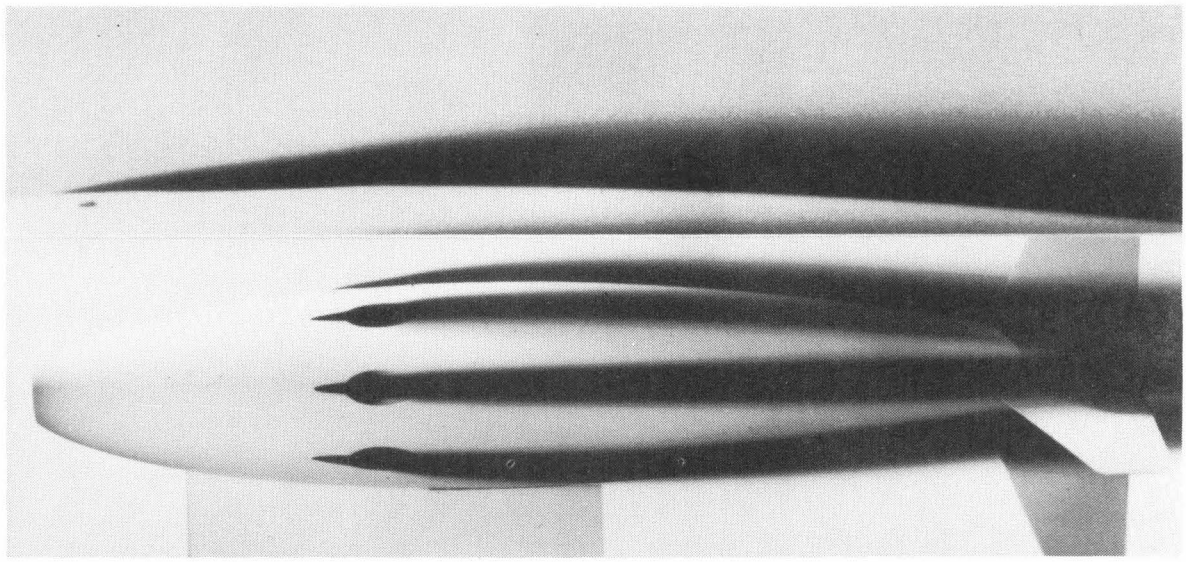

Fig. 8 - **Jet flow pattern** for a jet velocity ratio of 2.36. (Note: spraying of jet due to jet impingement on port)

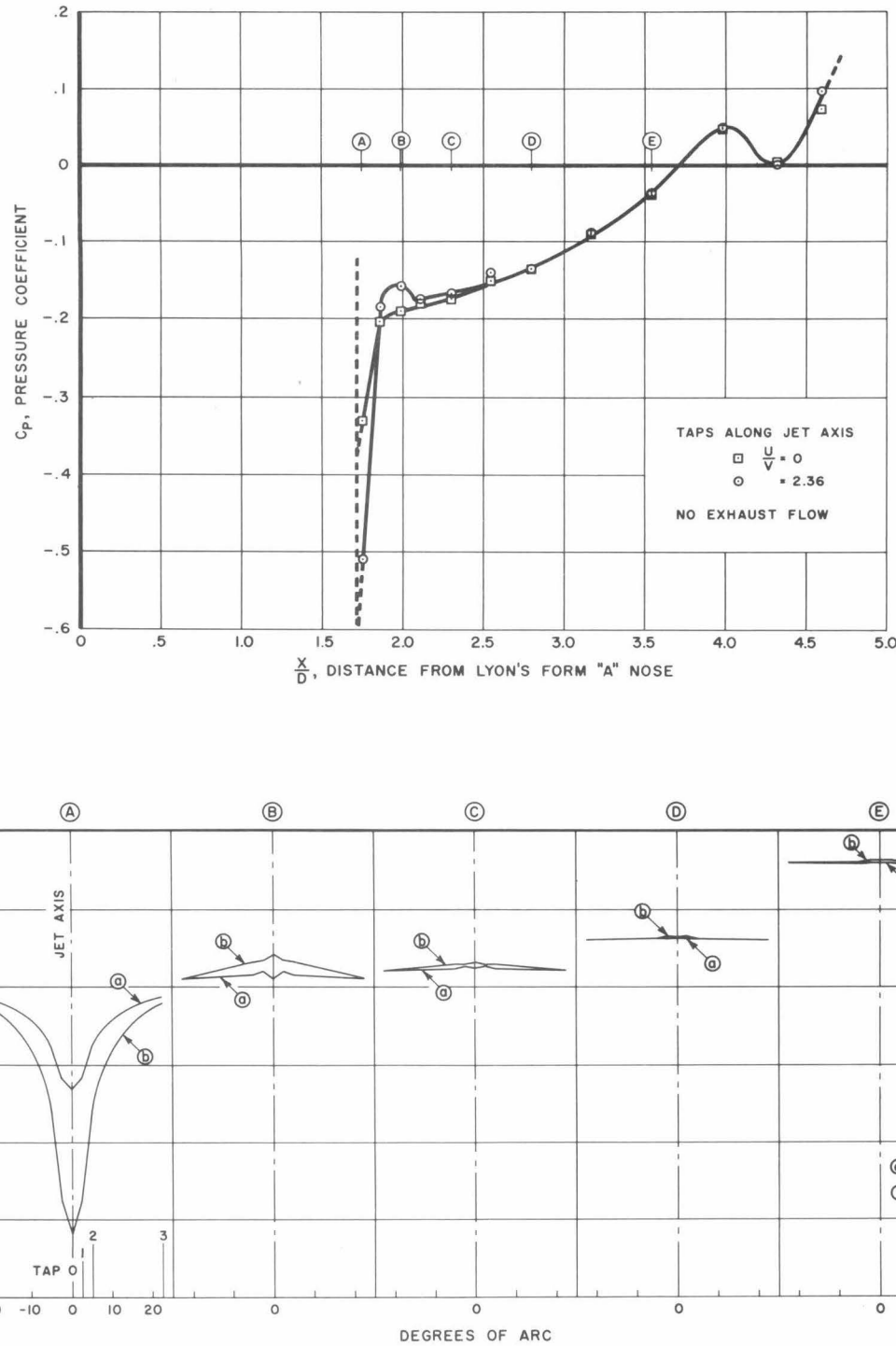

Fig. 9 - Model afterbody pressure distribution with and without jet flow. Tunnel velocity 30 fps.

conditions) can be make assuming geometrically similar body configurations and jet flow patterns. Model photographs and data from Ref. 4 indicate that approximately one-half of the jet cross section would encounter the exhaust port. If it is assumed that this portion of the jet is deflected from its flow direction to flow parallel to the port surface, the prototype axial impinging force is estimated to be 11% of the total body drag. This amounts to 330 lbs at a prototype velocity of 121 fps with a jet ratio of 2.36, Table II. These figures are for a jet-only (no exhaust) condition. If the exhaust gases were present the impinging force would probably be less than the estimated jet-only impinging drag force. Several different types of modifications have been suggested[4] to eliminate the jet impingement and the accompanying drag increase. A later section indicates that it is not possible to predict the effect of exhaust gas flow when used in conjunction with the jet impingement modifications.

It is interesting to note that the low pressure peak resulting from jet impingement does not appreciably affect the form drag. Actually, the sharpness of the peak and its position on the body tend to produce a very small decrease in the form drag.

Effect of Jet Flow on Afterbody Drag

The presence of the water jet adjacent to the afterbody surface causes local increased pressures, Fig. 9. The net effect of these higher local pressures is to make the effective pressure higher. Since the jets flow over the afterbody, the increase in effective pressure should result in a decrease in the form drag when the jets are operating. The calculated decrease is quite small, however. Figure 10 shows the change in calculated form drag coefficients of the model afterbody as a function of the jet-to-tunnel velocity ratio. It should be pointed out that the largest drag increment is of the same order of magnitude as the experimental scatter. Even though the jets seem to reduce the form drag, the calculated changes are insignificant. The largest change in form drag shown amounts to approximately 25 lbs for the prototype at top speed. This is less than 1% of the total prototype drag,[1] Table II.

The change in the model afterbody drag coefficients as a function of the jet-to-tunnel velocity ratio is shown in Fig. 10. The total drag

coefficient increases with increasing jet ratio. Since the form drag has been seen to decrease slightly, the increase in drag coefficient can be attributed to an increase in frictional drag. Figure 10 also shows the change in friction drag coefficient as a function of the jet velocity ratio. The increased friction drag can be attributed to increased fluid shear stress over the surface of the afterbody caused by the high velocity jets.

The following correlation has been made so that the model, jet-induced friction drag can be extrapolated to full scale. To make such a correlation several variables must be ascertained. They include the jet-influenced area, the effective (shear producing) velocity, the characteristic length, and the frictional drag force. The ratio of the model jet-influenced surface area to the cross section area is plotted in Fig. 11a as a function of the jet-to-tunnel velocity ratio. Note Appendix I for details of the area calculations. The friction force can be obtained from the friction drag coefficients, Fig. 10. The characteristic length for calculating Reynolds numbers was assumed to be the over-all body length. The effective velocity, however, could not be experimentally ascertained. By assuming that the jet-induced friction drag is similar to flat plate friction drag, it is possible to work the problem in reverse and to obtain a reasonable effective jet velocity ratio. The Schoenherr formula for flat plate friction drag was used to calculate the effective jet velocity ratio as a function of the actual jet velocity ratio, Fig. 11b. An estimate of the effective velocity ratio based on an extrapolation of the data from Ref. 4 indicates a ratio of less than 1.4 for a jet velocity ratio of 2.3. The calculated value shown in Fig. 11b is 1.2. Figure 12 shows the friction drag coefficient based on the calculated effective velocities as a function of Reynolds number. The Schoenherr flat plate friction curve upon which the effective velocities were based is also shown. Calculating the friction drag on the jet-influenced area for both jet and no jet conditions will show the change in drag force caused by jet flow.

The following illustrative calculations are based on a prototype velocity of 121 fps and a jet-to-body velocity ratio of 2.36. For an over-all length of 8.75 ft , a velocity of 121 fps and a kinematic viscosity of 12.2×10^{-6} (fresh water at 60° F) the prototype Reynolds number is 8.71×10^{7}. The Schoenherr friction drag coefficient[8] is 0.00211. For a jet-affected

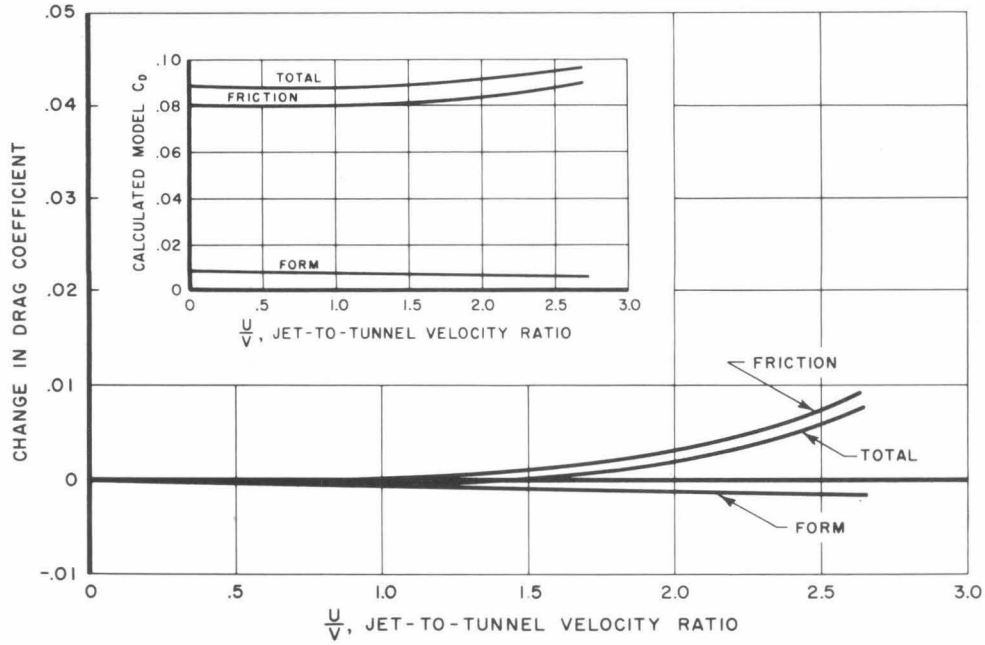

Fig. 10 - Experimental change in model afterbody drag coefficient versus jet-to-tunnel velocity ratio. No exhaust flow.

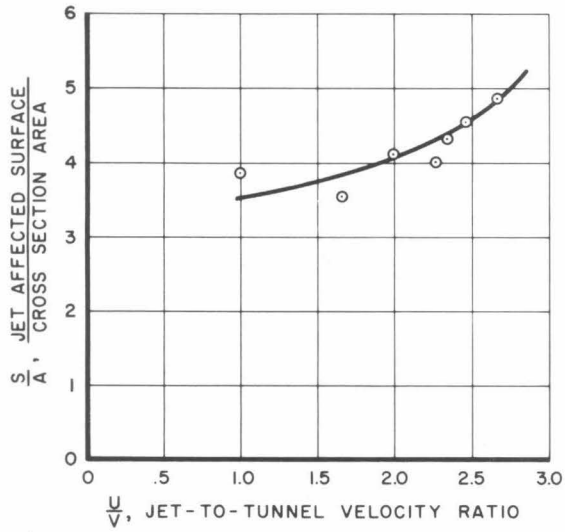

Fig. 11a - Area of body surface which is contacted by the water jet with no exhaust flow.

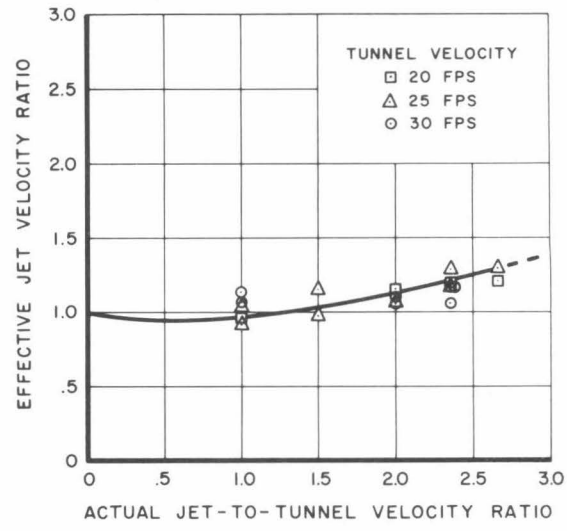

Fig. 11b - Effective jet velocity as based on Schoenherr formula. No exhaust flow.

area of 10.64 ft^2 and a water density of 1.938 slugs/ft^3, the friction drag force over this area is 320 lbs. The effective jet velocity, based on Fig. 11b, is 144 fps. The effective Reynolds number is 10.2×10^7. The Schoenherr friction coefficient is 0.00207. The friction drag force with the jets operating becomes 440 lbs. The increase in friction drag due to the jets is 120 lbs. This is approximately 4% of the total prototype drag at this speed,[1] Table II. Reference 4 suggests several possible modifications which would reduce this jet-induced friction drag. Later sections discuss the effect of the exhaust gas flow on the jet-induced friction drag.

Effect of Jet and Exhaust Flow on the Body Nose

Although simple jet flow does not affect the upstream area, the combined jet and exhaust flow cause a definite increase in the pressure upstream of the jet and exhaust ports. Figure 13a shows the effect of jet and exhaust flow on the pressure distribution of the model Mk 40 nose. These alterations in the pressure field increase the calculated nose form drag. Figure 13b shows the increase in model nose form drag coefficient as a function of the exhaust-to-tunnel velocity ratio. Data supplied this Laboratory by the Naval Ordnance Test Station shows a prototype noncondensable exhaust velocity ratio of approximately 0.8 at top speed. It is reasonable to assume that the condensable gases which the prototype discharges, also, are not instantly condensed. Comparison of photographs shown in Ref. 2 and those obtained in this Laboratory for relatively similar conditions, show considerable variation in the vicinity of the exhaust port. Actually similar flow patterns were observed when the simulated exhaust ratio was approximately twice the prototype noncondensable exhaust velocity ratio. Thus, the actual effective exhaust velocity is something greater than the noncondensable exhaust ratio. On the basis of Fig. 13b, for an effective exhaust velocity ratio of 0.8 at a jet ratio of 2.36, the increase in prototype form drag would be 280 lbs at a velocity of 121 fps. This force is 9% of the total drag force,[1] Table II. If the effective exhaust ratio in this region is as large as is indicated by the photographic comparison, the force is probably even greater than that calculated above. Because of the limited experimental range, a prediction of the actual prototype jet- and exhaust-induced form drag increase would not be valid. However, it seems reasonable to assume that the increase is in excess of the previously calculated 280 lbs, Table II.

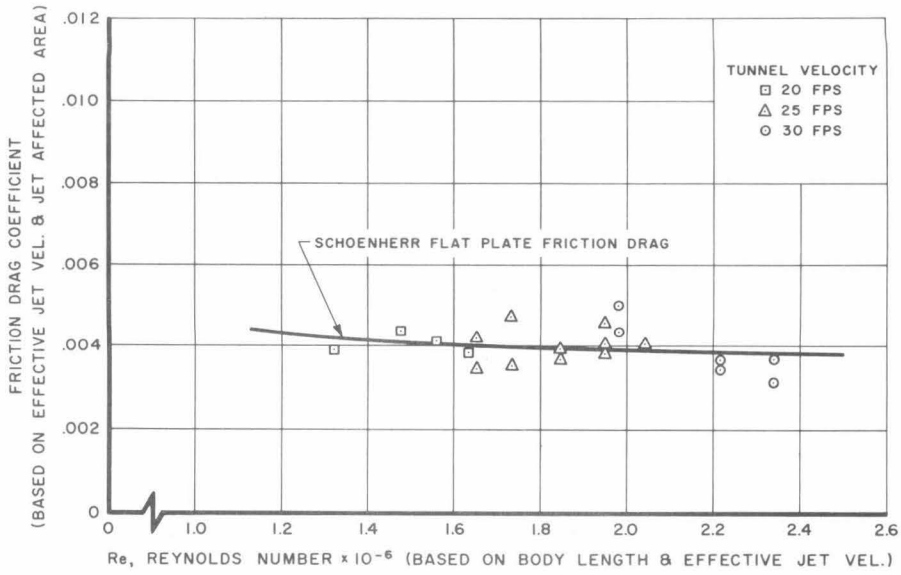

Fig. 12 - Correlation of model jet-induced friction drag with Schoenherr flat plate friction formula.

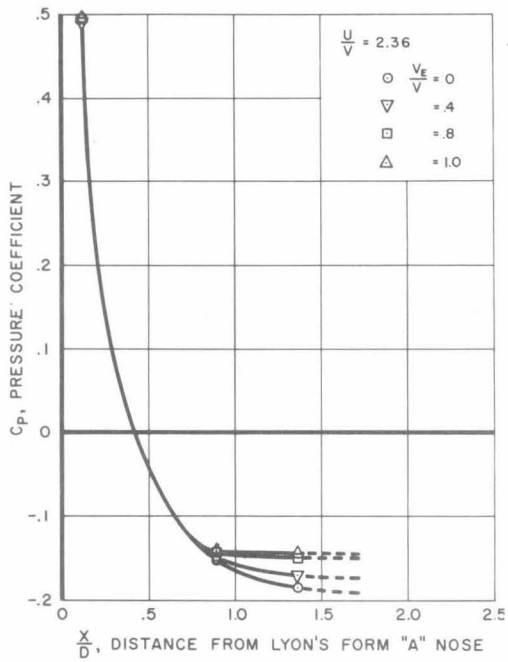

Fig. 13a - Model nose pressure distribution for various exhaust-to-tunnel velocity ratios. Jet ratio 2.36. Tunnel velocity 30 fps.

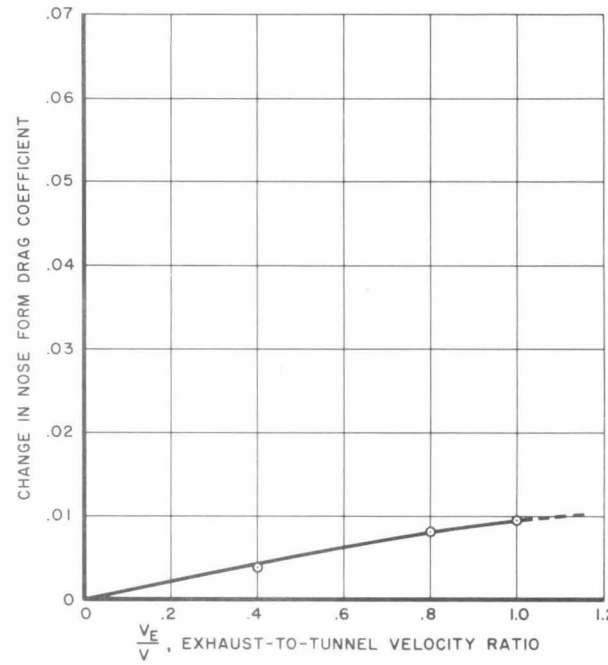

Fig. 13b - Effect of exhaust gas flow on calculated model nose form drag coefficient. Jet ratio 2.36. Tunnel velocity 30 fps.

Effect of Jet and Exhaust Flow on Jet-Induced Drag

Figure 14 shows the effect of exhaust gas flow on the model afterbody pressure distribution. As the exhaust velocity ratio is increased, the sharp pressure peak is reduced. At the same time, the pressure in the region immediately behind the port becomes lower for a considerable portion of the afterbody length. This is due to the presence of exhaust-filled cavities. The ratio of the surface area which the cavities enclose, to the model maximum cross section area, is shown in Fig. 15 as a function of the exhaust velocity ratio. These low pressure regions increase the calculated afterbody form drag of the model, Fig. 16. The total measured afterbody drag coefficient is shown as a function of exhaust velocity ratio in Fig. 16. The lower pressure area produced at an exhaust ratio of 1.0 extends over approximately 15% of the body length, Fig. 14. This means that the high energy, high velocity jet flows well above the body surface in this region. By the time the jet has returned close enough to affect the surface (indicated by a local increase in pressure) the effective velocity of the jet is greatly reduced. Thus, the jet-induced friction drag is probably reduced considerably. Figure 16 shows the model afterbody friction drag coefficient as a function of the exhaust velocity ratio. Figure 17 shows the changes in the drag coefficients which are caused by the combined jet and exhaust flow. For an exhaust ratio of 0.9, the decrease in the afterbody friction drag coefficient is greater than the increase in friction coefficient caused by the flow of the jet, Fig. 10. Actually, the small exhaust gas-filled cavities which occur at exhaust ratios greater than 0.8, eliminate a portion of the afterbody skin friction. The afterbody friction drag decrease is due to a reduction in the jet-induced drag plus a reduction in the skin friction drag. The effect appears to be an elimination of the jet-induced drag. Thus, it could be stated that the model jet-induced friction drag is reduced to a negligible value by the flow of exhaust gases.

The physical behavior which seems to explain the reduction in jet-induced drag should not be altered by larger exhaust flow rates. In fact, the higher exhaust ratios are apt to increase the extent of the gas-filled cavities and reduce the skin friction drag all the more. Consequently, it appears reasonable to assume that the prototype jet-induced drag is reduced by the presence of exhaust gases. Also, the normal body skin friction drag is less than the bare body friction drag. Thus, it appears that the prototype jet-induced friction drag is reduced to a negligible amount.

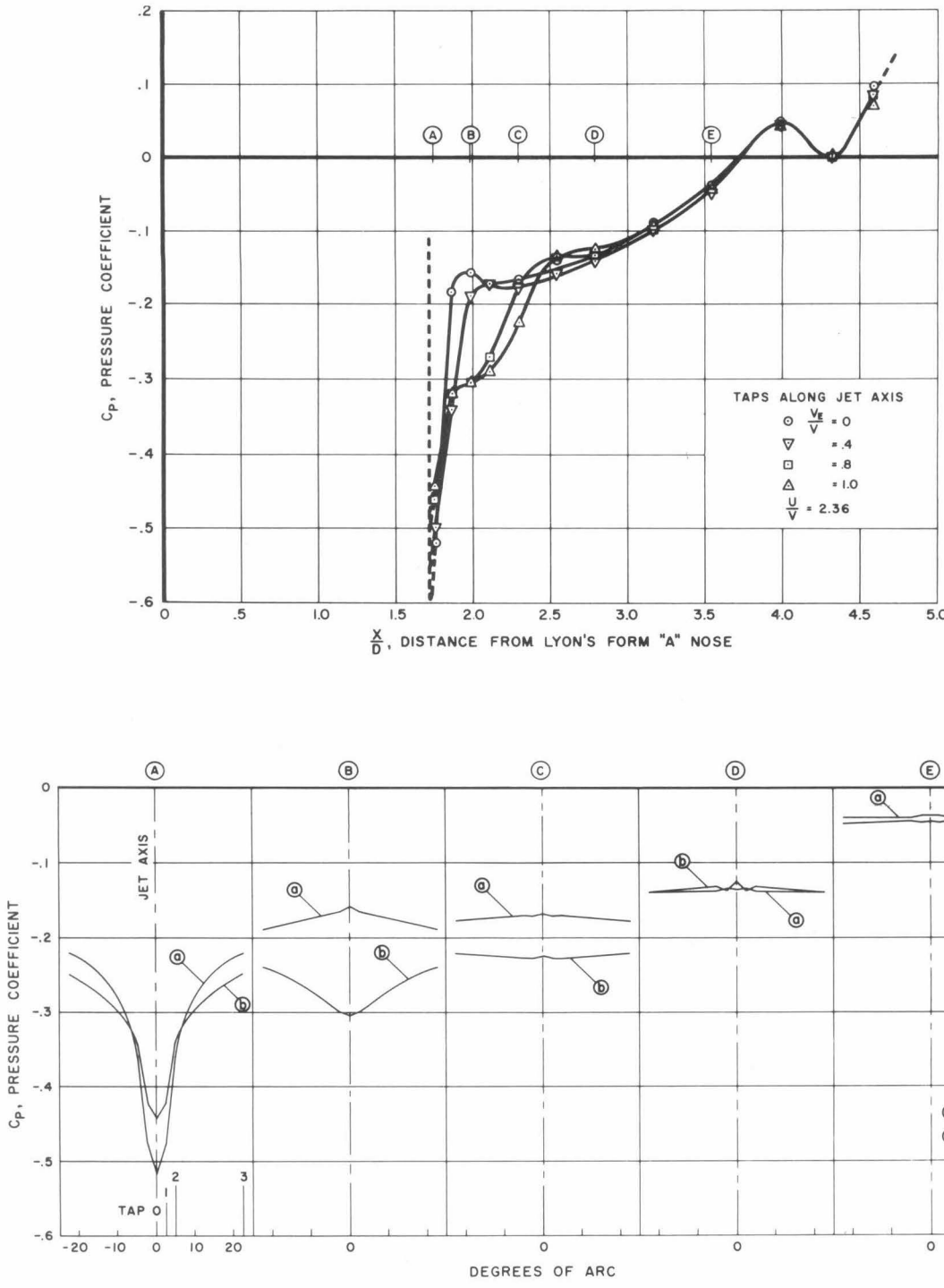

Fig. 14 - Model afterbody pressure distributions for various exhaust velocity ratios. Jet ratio 2.36. Afterbody with fins. Tunnel velocity 30 fps.

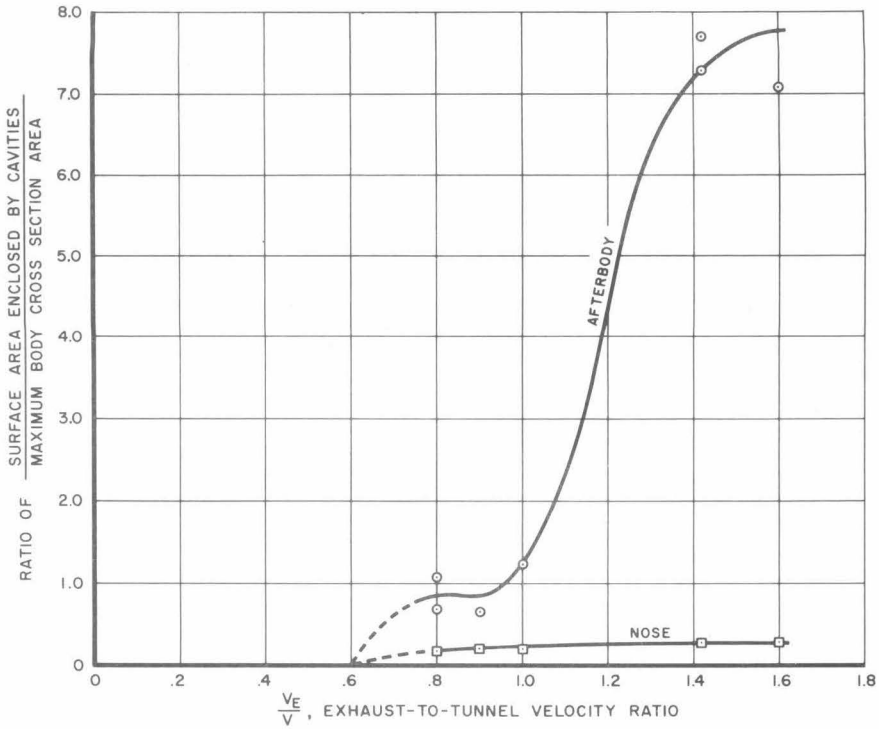

Fig. 15 - Surface area enclosed by exhaust filled cavities versus the exhaust velocity ratio. Jet velocity ratio 2.36. Tunnel velocity 30 fps.

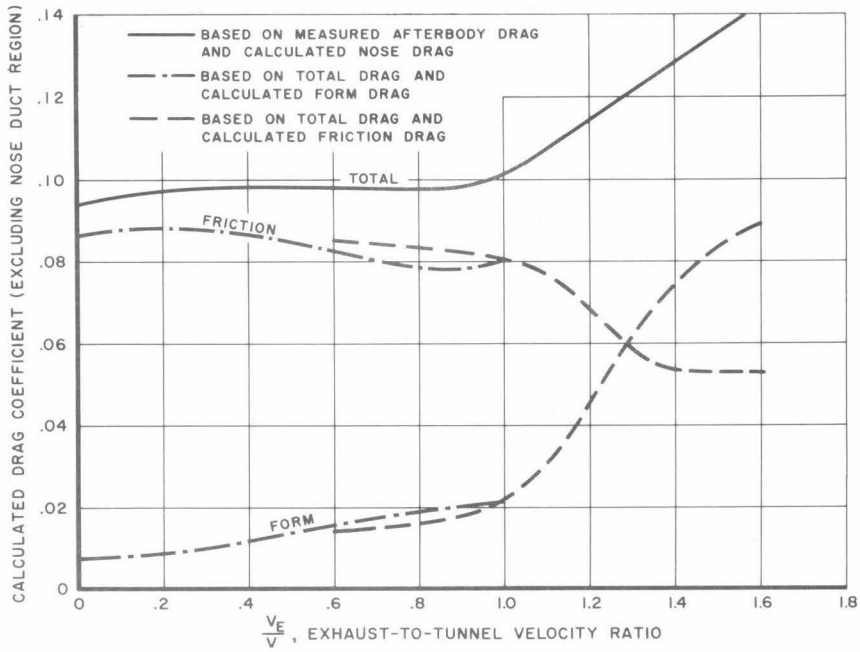

Fig. 16 - Analysis of the effect of the exhaust flow on the components of the total model drag coefficient.
Jet velocity ratio 2.36. Tunnel velocity 30 fps.

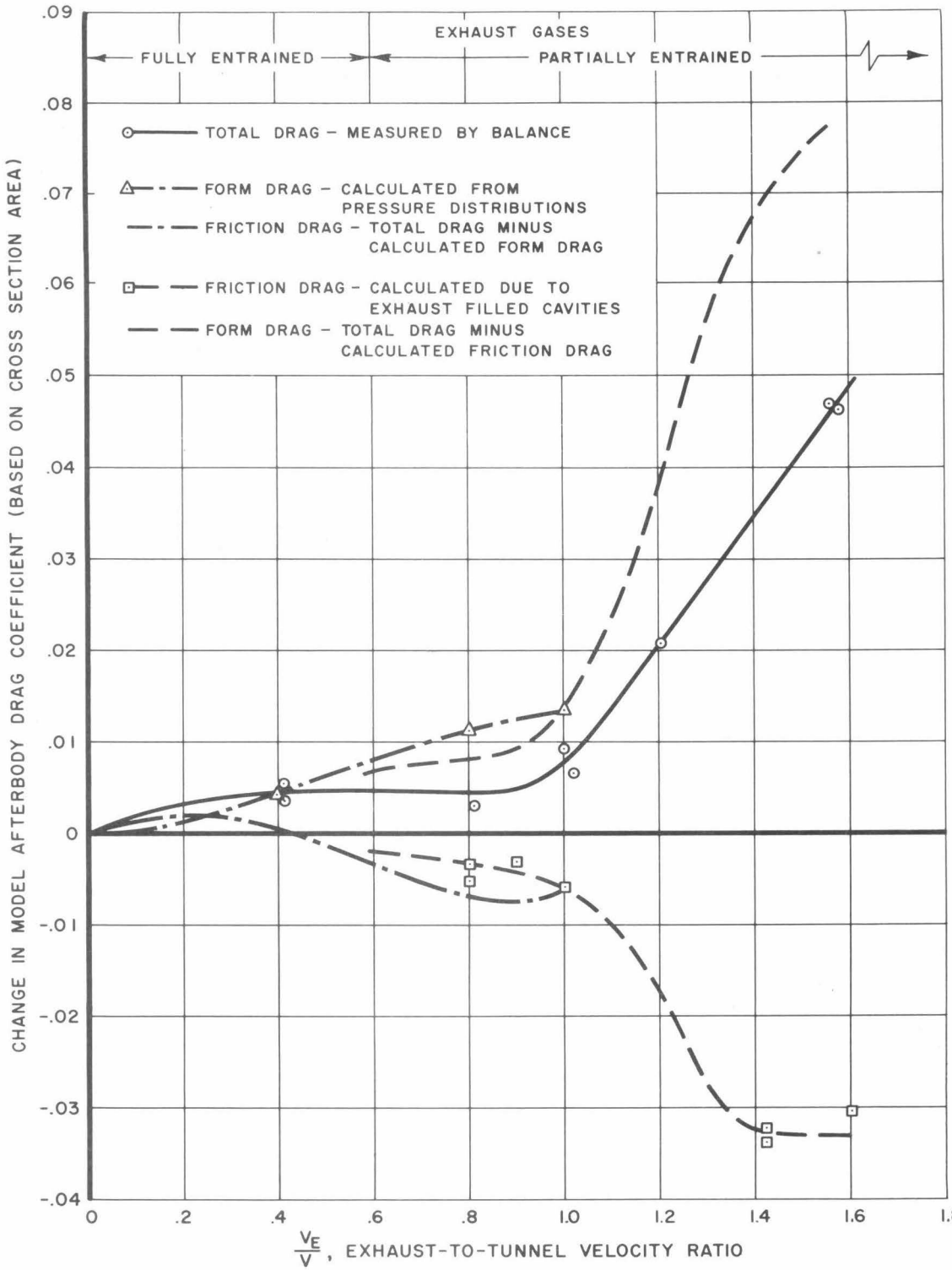

Fig. 17 - Change in model afterbody drag coefficients versus the exhaust-to-tunnel velocity ratio for a jet velocity ratio of 2.36. Tunnel velocity 30 fps.

The reduction of the model afterbody friction drag due to the presence of exhaust-filled cavities was calculated on the basis of the surface area enclosed by the cavities, as shown in Figs. 18 and 19. The calculated reduction in model drag coefficient is shown in Fig. 17 (dashed curve). At low exhaust ratios the calculated reduction in friction drag due to the exhaust cavities does not account for the complete reduction in friction drag as obtained from model force and pressure data. This difference can be explained as follows. For convenience, the water jet has been considered to have a constant effective velocity. Actually due to the turbulent diffusion of the jet, the effective velocity near the exhaust port is greater than that near the tail of the model. Thus the over-all effective jet velocity is less than the actual effective jet velocity near the port. Since the jet is separated from the model afterbody by the exhaust-filled cavities near the port, the reduction in jet-induced friction drag will be greater than that estimated on the basis of the average effective jet velocity. The exact amount of this difference can not be calculated because of the complex jet and exhaust diffusion patterns. However, the difference between the two friction drag curves, Fig. 17, is an indication of the actual error resulting from the simplifying assumption of an average effective jet velocity. This discrepancy in the friction drag force coefficient amounts to a discrepancy in the prototype friction drag of 2% of the total drag.

Effect of Jet and Exhaust Flow on the Total Afterbody Drag

For exhaust ratios in the prototype noncondensable-ratio range (up to 0.8), the calculated and estimated form drag increases and friction drag decreases do not account for the increases in total drag reported in Ref. 1. As has been mentioned, the actual prototype exhaust velocity ratio is probably larger than that based on the noncondensable exhaust flow. Since the rate of condensation of the gases is not known, it is difficult to duplicate full-scale conditions over the entire afterbody. The following analysis points out the various features of the simulated exhaust flow for a jet velocity ratio of 2.36 and correlates them with definite effects on the afterbody drag.

For small exhaust velocity ratios (0.5), Fig. 18a, the exhaust gases do not appear to have sufficient energy to penetrate the ambient flow. Actually, the gases are removed from the port by entrainment into the water jet

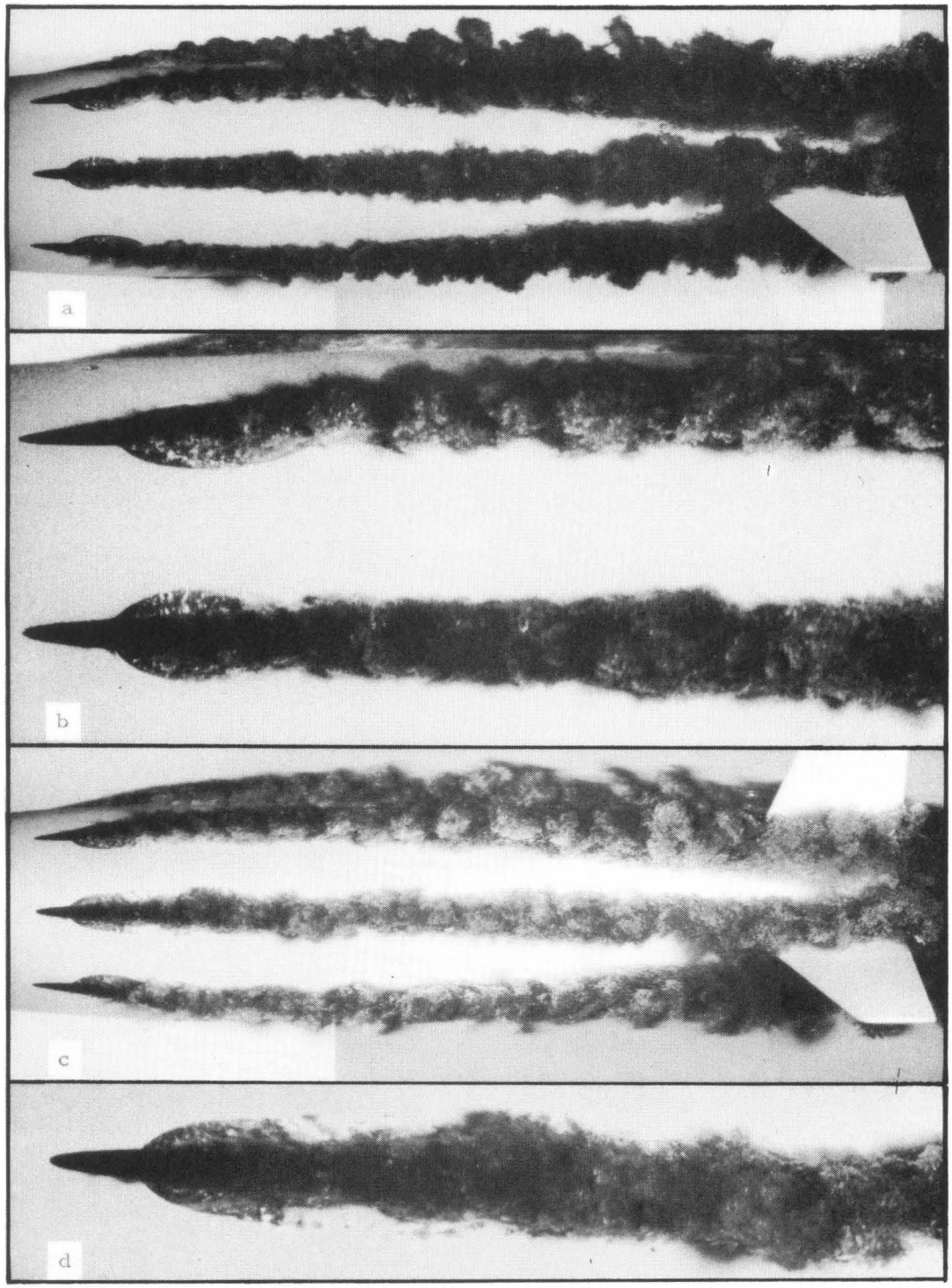

Fig. 18 - Entrainment of exhaust gases into jet stream for a jet velocity ratio of 2.36. Tunnel velocity 30 fps.
(15 microsecond flash duration photographs)

a) b) Exhaust ratio 0.5

c) d) Exhaust ratio 0.8

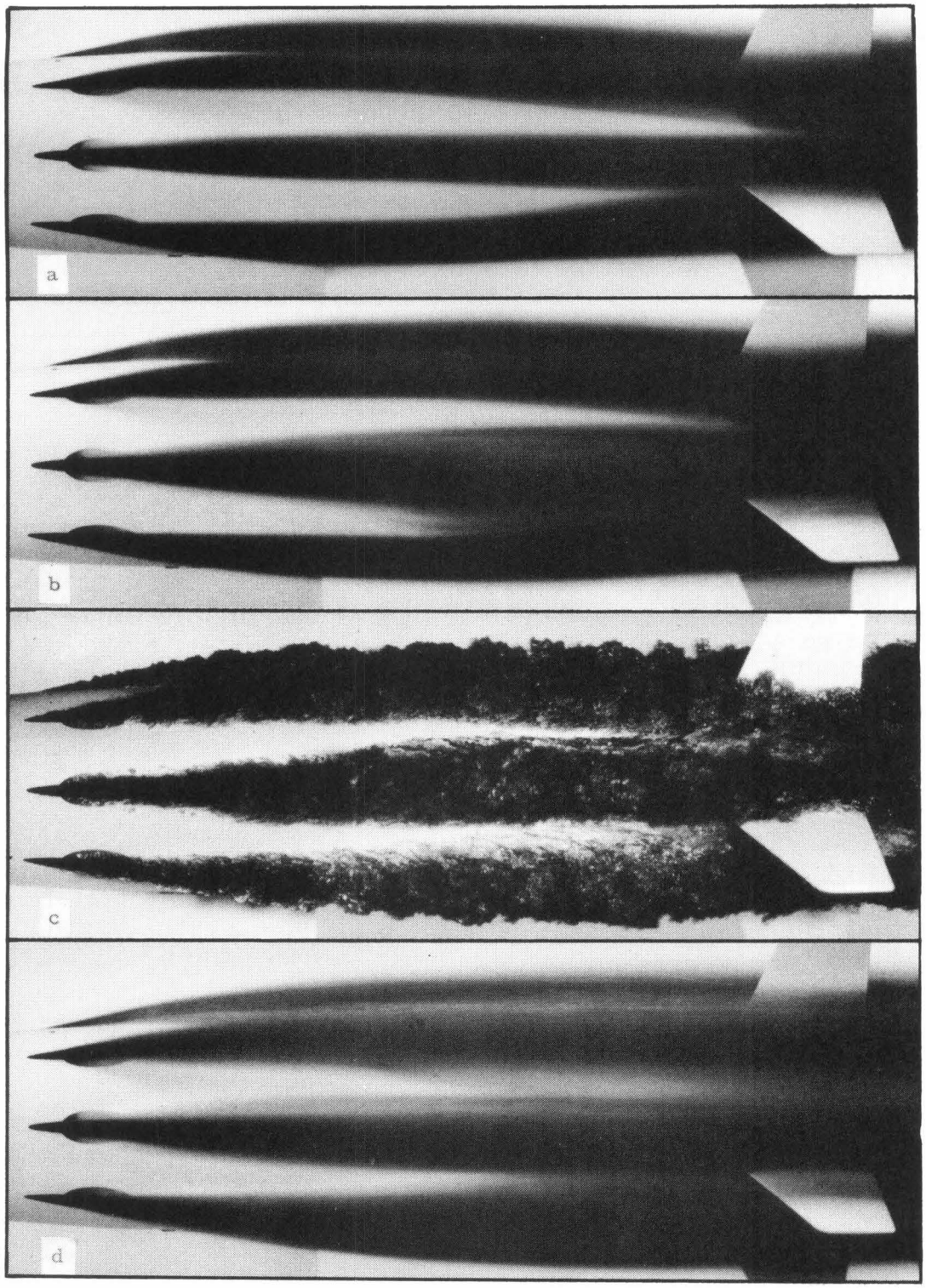

Fig. 19 - Jet and exhaust flow patterns for high model exhaust velocity ratios.
Jet ratio 2.36. Tunnel velocity 30 fps.

a. Exhaust velocity ratio 0.9
b. Exhaust velocity ratio 1.4
c. Exhaust velocity ratio 1.4 (15 microsecond flash photograph)
d. Exhaust velocity ratio 2.2

stream. Thus, there is no actual penetration of the free stream by the exhaust gases. Figure 18b shows some of the exhaust gases being swept into the jet stream. The remaining gases in the port probably tend to flow between the jet and the rear surface of the exhaust port. The impact of the high velocity jet on the gases probably causes additional entrainment into the jet stream. It is by these two processes that the exhaust gases probably are removed from the port. With an increase in the exhaust ratio the afterbody form drag increases only a small amount as long as the gases are fully entrained, Fig. 17. If the water jet arrangement were modified to eliminate the jet impingement,[4] the exhaust gases would probably not be as completely entrained for comparable velocity ratios. The gases would flow under the jet and they would be discharged unentrained. These gases would probably form cavities over the entire length of the afterbody extending the exhaust pressure to these areas. Although pressures in the cavities would probably be slightly higher than those which occur when the jet impinges, the cavities would cover a much larger portion of the afterbody. Thus, the form drag might increase under the conditions with the modified jet. The presence of these gas cavities is similar to the effect caused by exhaust rates which are greater than entrainment rates. This occurs on the unmodified configuration for exhaust ratios in excess of 0.6. For an exhaust ratio of 0.8, the unentrained gases form a small cavity in the low pressure region below the jet, Figs. 18c and 18d. The pressure distribution, Fig. 14, shows an extended low pressure region due to the exhaust gas-filled cavity. The afterbody form drag, Fig. 17, will be greater than for the lower exhaust ratios. Since the small cavity resulting from an exhaust ratio of 0.8 occurs near the maximum body diameter, the effect on the drag is rather small. If the cavity were slightly longer or occurred on the afterbody, the increase in form drag would be much greater. The small cavities, also, reduce the afterbody friction drag so that the net increase in total afterbody drag is small for exhaust ratios less than 1.0.

Model exhaust velocity ratios greater than 0.9 produce pronounced and extensive gas-filled cavities, Fig. 19. For these cases the exhaust rate is much greater than the entrainment rate. The large area covered by the cavities results in a large reduction in the afterbody

friction drag. However, the cavities undoubtedly cause the major portion of the afterbody to experience pressures which are much less than normally occur. The presence of the lower pressures on the afterbody cause increases in the form drag. Figure 17 shows the large increase in total drag coefficient which the higher exhaust ratios cause. The actual increase in model afterbody form drag is greater than this because the friction drag decreases as the exhaust ratio increases. Thus, it can be seen that as the exhaust gas-filled cavities extend over the model afterbody, the drag increases rapidly. If the jets were modified to eliminate impingement, the gas cavities would probably be longer and narrower than those shown in Fig. 19. The effect of high exhaust ratios in conjunction with modified jets cannot be predicted from the present data. It should be emphasized that the preceding discussion applied only to the experimental model Mk 40 with air simulated gas exhausts for a jet velocity ratio of 2.36.

A qualitative analysis of the jet- and exhaust-induced drag indicates large model drag forces can be attributed to the flow of exhaust gases over the body surface. The jet-induced friction drag appears to be eliminated by the flow of the exhaust gases. Since the major increase in model afterbody drag has been shown to be due to an increase in form drag plus a small reduction in friction drag, it would seem to be an easy matter to obtain quantitative data which could be applied to the prototype. As has been pointed out, the prototype exhaust gases are approximately 50% condensable; however, the rate of condensation is not known.[1] A comparison of model flow patterns, Fig. 19, and prototype flow patterns[2] around the exhaust ports, indicates that the actual prototype exhaust velocity ratio is approximately 2.0. This is reasonable, if it is assumed that there is no condensation of the exhaust gases in the exhaust ducts. As might be expected, a comparison of these high exhaust ratios near the tail is not satisfactory. A ratio of 1.0 might present a better representation of the prototype flow pattern near the tail. However, the large exhaust ratio upstream will have an effect on the pressure near the tail. Thus, any attempt to correlate drag data on the basis of the apparent exhaust ratios would not be rigorous. Another unknown parameter is the turbulence level of the jets which would affect the rate of exhaust entrainment. These factors prohibit a direct correlation of the present data to full-scale

performance.

By making some conservative assumptions it is possible to utilize the actual model data to estimate the magnitude of the jet- and exhaust-induced drag. If it is assumed that the condensable gases are instantly condensed in the exhaust port and that the noncondensable gases are fully entrained, an estimate of the lower limit of the jet- and exhaust-induced drag can be obtained. It is also assumed that the form drag is independent of Reynolds number. For a prototype velocity of 121 fps, a jet velocity ratio of 2.36 and an exhaust velocity ratio of 0.8, the increase in afterbody form drag force would be 390 lbs. The decrease in afterbody friction drag force would be 115 lbs. The net lower limit of the jet- and exhaust-induced afterbody drag force would be 275 lbs. This is 9% of the total prototype drag force.[1] This is a conservative estimate of the induced drag force if the exhaust rate is greater than the prototype exhaust entrainment rate.

It is quite apparent that the over-all effective exhaust ratio is not 2.0. However, it is conceivable that one-third of the condensable gases might remain in the exhaust-filled cavities long enough to cause an increased effect on the drag. If it is assumed that the effective exhaust velocity ratio is one-third greater than the noncondensable exhaust ratio, an induced form drag increase of 668 lbs would result for the same conditions as above. The afterbody friction drag would be reduced 164 lbs. This assumption results in a net jet- and exhaust-induced afterbody drag of 504 lbs. This is 17% of the total prototype drag force,[1] Table II. These estimates give an idea of the magnitude of the jet- and exhaust-induced afterbody drag on the prototype Mk 40 X-1 under noncavitating conditions. To these must be added the estimated increase in nose form drag induced by exhaust flow (266 lbs for the instantly condensable assumption; 316 lbs for the other assumption). The estimated over-all jet- and exhaust-induced drag increase is greater than 541 lbs., and possibly 820 lbs. These are 18 and 28% of the total drag force,[1] Table II. The larger figure is approximately equal to that shown in Ref. 1 for "water jet friction" and "two phase drag" at top speed. It should be pointed out that the steepness of the induced drag curve, Fig. 17, indicates that small changes in exhaust and/or condensation rate will cause large changes in the estimated induced drag.

Another approach to the problem of estimating the prototype jet- and exhaust-induced drag is to estimate the prototype pressure distribution on the basis of the available model data and the available photographs of the operating prototype.[1, 2] Although the photographs are of a low-speed run with a liquid metal propellant, they indicate the nature of the exhaust cavities and the extent to which the cavities are dispersed. With these features in mind, an estimated prototype pressure distribution is presented, Fig. 20. The large estimated low pressure region over the afterbody is due to the presence of large surface-attached, exhaust-filled cavities which originated at the exhaust ports. The magnitude of this low pressure is estimated on the basis of similar measured model pressures for exhaust velocity ratios of 0.8 and 1.0. The position and manner of pressure recovery is estimated on the basis of the nature of the dispersion of the exhaust cavities during the low-speed test runs.[1, 2] As indicated by model photographs, the limits of the exhaust-filled cavities are not fixed. Surface ripples and actual surface entrainment cause the outline of the cavities to vary continuously. Thus, the exhaust cavity pressure does not occur over the entire body surface which appears to be enclosed by the cavity. The estimated afterbody circumferential pressure distributions, Fig. 20, are not flat-topped for the above reason. The estimated amount of pressure recovery was based on the amount of pressure recovery which occurs on cylindrical body sections downstream of the collapse of vapor cavitation which has comparable minimum pressures and comparable lengths of flow separation.[9]

On the basis of the estimated prototype pressure distribution, the calculated jet- and exhaust-induced afterbody form drag is 1071 lbs. The calculated induced nose form drag is 409 lbs. The total jet- and exhaust-induced form drag is 1480 lbs. This is 50% of the total prototype drag,[1] Table II. The friction drag is estimated to be reduced 562 lbs. The net jet- and exhaust-induced drag force is 918 lbs. This is 31% of the total prototype drag,[1] Table II. This net induced drag force, based on the estimated prototype pressure distribution and exhaust flow pattern, agrees within 3% of the actual reported jet- and exhaust-induced drag forces.[1]

As has been seen, the jet- and exhaust-induced drag forces appear to be a large percentage of the total drag force, Table II and Ref. 1. Thus,

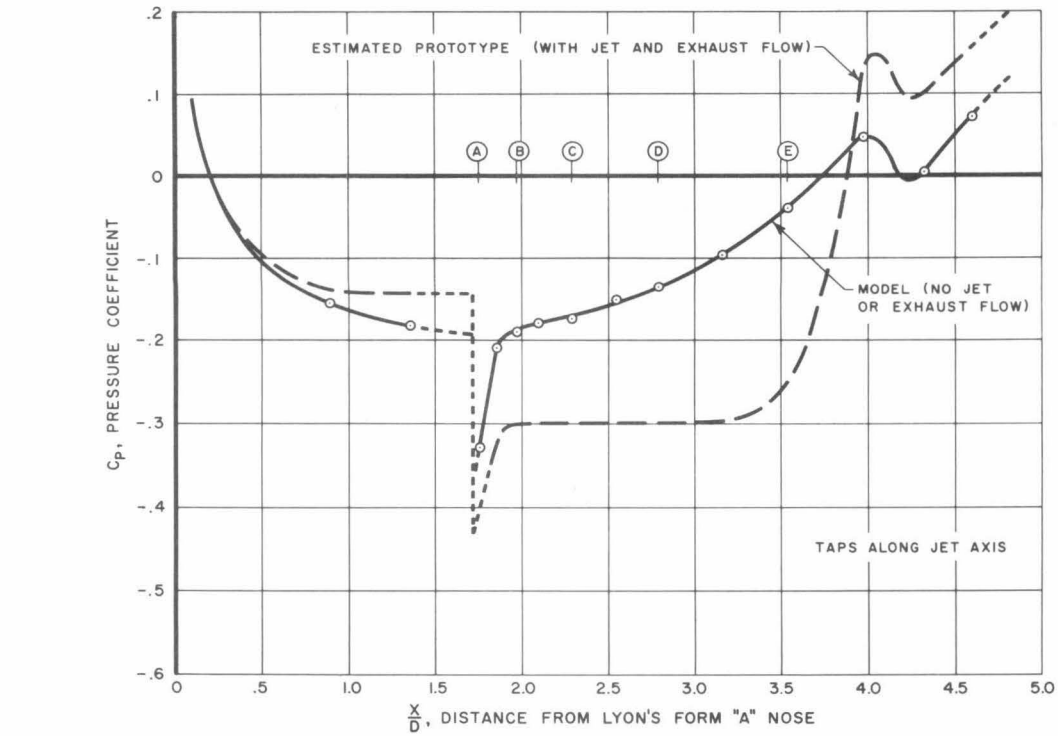

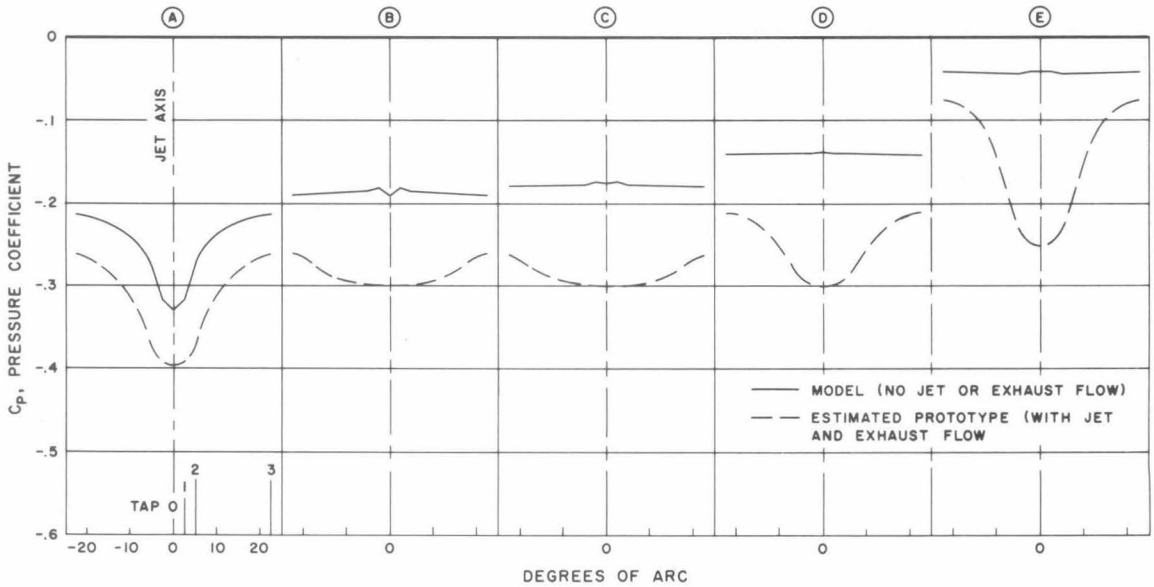

Fig. 20 - Estimated prototype TTV Mk 40 X-1 pressure distribution at top speed with water jets and gas exhausts operating. Model pressure distribution shown for comparison.

a reduction in the jet- and exhaust-induced drag seems to be the most fruitful field for improvement in prototype performance. A full condensing fuel system has been suggested[1,2] as a possible modification. The ducting of the exhaust gas to the tail has also been suggested.[1,2] It seems conceivable that a modification of the present exhaust port system might make a significant improvement in the induced drag forces. Another approach to the problem is the modification of the jet arrangement to improve the entrainment rate or to limit the exhaust flow pattern .

Note Appendix IV for details of the effect of exhaust gas flow without water jets on the flow patterns and the afterbody drag.

Effects of Cavitation Based on Model Data

Performance specifications of the prototype require a velocity of 80 knots (135 fps) at a depth of 12 ft. These conditions represent a cavitation number of 0.16. Noting the pressure distributions in Fig. 14, it appears that 15% of the model body length has pressure coefficients which are lower than -0.16 for a jet velocity ratio of 2.36 and an exhaust velocity ratio of 1.0. On this basis it can be inferred that cavitation would probably occur over this region and extend further toward the tail. The presence of the exhaust gases would probably extend the region of cavitation even further toward the tail. For a cavitation number of 0.16 large form drag increases could be expected from the combined jet and exhaust flow and cavitation.

The prototype test vehicle actually encountered much higher cavitation numbers (0.33 to 0.37) in tests at the Naval Ordnance Test Station.[1] The present data does not cover a sufficient range of exhaust ratios to make a valid extrapolation to full scale. It would seem, on the basis of the pressure distribution, Fig. 14, that the only region of cavitation for these cavitation numbers is immediately behind the exhaust port. Since this region is filled with exhaust gases, Fig. 19, the presence of cavitation is precluded. However, this exhaust ratio (1.0) is not realistic in this region. The actual effective ratio is probably near 2.0. The exact effect of this larger exhaust ratio is not known from the present data. Also, this does not consider possible vortex cavitation from the fins, or cavitation of the supporting struts or cable shoes of the NOTS Underwater Cable Range version of the prototype. Laboratory tests[10] show

an incipient cavitation number of approximately 2.0 for one type of cable shoes.

Extrapolation of Results to Mk 40 with a Cylindrical Midsection

The preceding discussions have been based on a Mk 40 of the basic Lyon's Form "A" shape. This section discusses the effect of adding a cylindrical midsection to the basic shape.[1, 2] The sections on nose contour, exhaust-induced nose form drag and cavitation characteristics should apply, in general, to the configuration with the cylindrical midsection. The jet-only-induced drag would probably be slightly higher for this configuration. The exhaust gas flow would probably eliminate the jet-induced drag as it appears to do for the basic shape. More of the exhaust gases are apt to be condensed before they have as large an effect on the drag. Thus, the jet- and exhaust-induced form drag is probably less than for the basic configuration. However, the skin friction drag and the bare body form drag are considerably higher than for the basic configuration.

Summary of Results

The preceding sections have presented an analysis of experimental data as it concerns the external hydrodynamics of the TTV Mk 40 X-1. Analysis of the model pressure distribution indicates that the flow conditions over the nose might be improved by modifying the nose contour. An improvement of this sort would probably reduce the bare body form drag. It was shown that there is a small increase in the model afterbody drag with operation of the water jets only. A correlation of this data was extrapolated to indicate a 120-lb frictional drag increase (4% of total drag[1]) at a speed of 121 fps for a jet velocity ratio of 2.36. The operation of simulated gas exhausts reduced the model jet-induced drag to a negligible value. Thus, it was assumed that the prototype exhaust flow would all but eliminate the full-scale, jet-induced drag. The gas exhaust was estimated to increase the prototype nose form drag approximately 330 lbs (11% of total drag[1]). The flow of gases over the afterbody was found to increase the model afterbody drag considerably. A direct extrapolation of the jet- and exhaust-induced drag force would probably be in excess of 541 lbs (18% of total drag[1]) and possibly as high as 820 lbs (28% of

total drag[1]). The present data does not allow any more definite extrapolation. An estimated prototype pressure distribution and exhaust flow pattern were predicted. The jet- and exhaust-induced drag force based on these estimates would be 918 lbs (31% of total drag[1]). These results indicate the principal sources and the order of magnitude of the performance limiting drag forces. The present data indicated that under specified performance conditions the prototype body would probably cavitate. It was impossible to state whether the cable range test runs would experience cavitation or not. Note Table II for a summary of the extrapolated and estimated prototype drag forces.

Possible Fields for Future Study

It is realized that the body configuration was frozen early in the history of the Mk 40, restricting modifications which might have been later deemed desirable. However, a suitable study of the optimum configuration for nose-ducted bodies should be investigated in connection with possible refinements of the present configuration, as well as for use in the design of other high-speed torpedoes.[1,2]

The most apparent field for study is in the manner of discharge of exhaust gases. As mentioned in Refs. 1 and 2, it is desirable to exhaust the gases near the present exhaust location. On this basis a redesign of the exhaust port system might better control the exhaust gases so that they would not have such a large effect on the form drag. Rearrangement of the exhaust and jet port systems might also improve the control and entrainment of the exhaust gases. A basic study of the mechanics of gas-liquid entrainment would be of value if the gases are to be exhausted over such a large portion of the body. These general fields of study are suggested with an eye to the eventual development of high-performance torpedoes.

TABLE I

Summary of Model Drag Data

$R_e = 1.99 \times 10^6$

	Nose C_D	Afterbody C_D	Nose and Afterbody C_D
No Jet or Exhaust Flow			
Form Drag[a]*	[b] -.0276	+.0366	+.0090
Friction Drag[c]	+.0191	+.0606	+.0797
Form and Friction Drag	-.0085	+.0972	+.0887
Experimental Drag[d]	No data	+.0990	No data
Jets Only (Jet velocity ratio 2.36)			
Change of Form Drag[a]	0	-.0014	-.0014
Change of Friction Drag[e]	No data	+.0063	No data
Change of Total Drag[d]	No data	+.0049	No data
Jet and Exhaust Flow (Jet velocity ratio 2.36; Exhaust velocity ratio 0.8)			
Change of Form Drag[a]	+.0082	+.0114	+.0196
Change of Friction Drag[e]	No data	-.0070	No data
Change of Total Drag[d]	No data	+.0044	No data

*(a) Calculated from pressure distributions (Fins Curve B).

(b) + = drag force; - = propelling force.

(c) Calculated from Schoenherr Formula (assuming turbulent flow on fins).

(d) Measured by afterbody drag balance.

(e) Obtained by subtracting the form drag from the total drag.

(f) Extrapolated, assuming form drag constant for all Reynolds numbers.

(g) Based on effective jet velocity and the jet-affected area.

(h) Assuming instant condensation of the condensable gases and complete entrainment of the noncondensable gases.

(i) Assuming one-third of the condensable gases remain noncondensed long enough to increase the drag.

TABLE II

Summary of Extrapolated and Estimated Prototype Drag

$R_e = 8.71 \times 10^7$; Prototype Drag = 2950 lbs[1]

(Superscripts are defined as in Table I)

	Nose		Afterbody		Nose and Afterbody	
	C_D	Force (lbs)	C_D	Force (lbs)	C_D	Force (lbs)
No Jet or Exhaust Flow (Extrapolated)						
Form Drag[a,f]	-.0276	- 941	+.0366	+ 1248	+.0090	+ 307
Friction Drag[c]	+.0106	+ 362	+.0288	+ 982	+.0394	+ 1344
Form + Friction Drag	-.0170	- 579	+.0654	+ 2230	+.0484	+ 1651
Jets Only (Jet velocity ratio 2.36) (Extrapolated)						
Change of Form Drag[f]	0	0	-.0014	- 48	-.0014	- 48
Change of Friction Drag[g]	No data	-	+.0035	+ 120	No data	-
Change of Form and Friction Drag	No data	-	+.0021	+ 72	No data	-
Jet Impinging Drag		+ 330				
Jet and Exhaust Flow (Estimated)						
A. Jet velocity ratio 2.36; Exhaust velocity ratio 0.8[h]						
Change of Form Drag	+.0082	+ 280	+.0114	+ 390	+.0196	+ 670
Change of Friction Drag	-.0004	- 14	-.0034	- 115	-.0038	- 129
Change of Total Drag	+.0078	+ 266	+.0080	+ 275	+.0158	+ 541
Change of Total Drag + Bare Body Total Drag	-.0092	- 313	+.0734	+2505	+.0642	+ 2192
(Does not include the drag forces in the nose duct)						
B. Jet velocity ratio 2.36; Exhaust velocity ratio 0.8[i]						
Change of Form Drag	+.0097	+ 330	+.0196	+ 668	+.0293	+ 998
Change of Friction Drag	-.0004	- 14	-.0048	- 164	-.0052	- 178
Change of Total Drag	+.0093	+ 316	+.0148	+ 504	+.0241	+ 820
Change of Total Drag + Bare Body Total Drag	-.0077	- 263	+.0802	+2734	+.0725	+ 2471
(Does not include the drag forces in the nose duct)						
C. Based on an estimated prototype pressure distribution and exhaust flow pattern						
Change of Form Drag	+.0120	+ 409	+.0314	+1071	+.0434	+ 1480
Change of Friction Drag	-.0004	- 14	-.0161	- 548	-.0165	- 562
Change of Total Drag	+.0116	+ 395	+.0153	+ 523	+.0269	+ 918
Change of Total Drag + Bare Body Total Drag	-.0054	- 184	+.0807	+2753	+.0753	+ 2569
(Does not include the drag forces in the nose duct)						

APPENDIX

I. Qualitative Analysis of Jet and Exhaust Flow Patterns

Figure 21 shows the effect of various jet-to-tunnel velocity ratios on the water jet flow pattern of a model Mk 40. For low jet ratios, the jet flows along the surface of the afterbody as a streamline. For a jet ratio of 1.0, Fig. 21a, the top jet shows a sharp discontinuity near the rear of the exhaust port. This is due to the impingement of the jet upon the exhaust port. At higher velocity ratios, Fig. 21b, the visible results of jet impingement are not quite so apparent. Figures 21c and 21d are for the same jet ratio. Figure 21d illustrates the highly turbulent nature of the jets. It is quite evident from these figures that the water jet flows over the surface of the afterbody for nearly the entire length of the afterbody. The effect of the jet flow on the body is discussed in the text and in the following two sections.

Figure 22 shows the effect of increasing jet velocity ratio on the jet and exhaust flow patterns for an exhaust velocity ratio of approximately 1.4. The low jet ratio results in very little, if any, exhaust entrainment, Fig. 22a. Actually, the jet appears to flow over the cavity created by the exhaust gases. For a jet ratio of 2.0, Fig. 22b, the water jet seems to mix quite completely with the exhaust gases except adjacent to the body. The extent of the excess gases which flow over the edge of the exhaust port, Fig. 22c, is very similar to that for a jet ratio of 1.0, Fig. 22a. Thus, the rate of entrainment in the vicinity of the exhaust port is probably similar for a jet ratio of 1.0 and 2.0. However, the gas entrainment over the afterbody is very noticeable for a jet ratio of 2.0. For a jet ratio of 1.0 there is no observable gas entrainment along the afterbody. For a jet ratio of 2.36, Figs. 22d and 22e, the exhaust port entrainment rate seems to be greater than for a jet ratio of 2.0. The actual spread of the jet and exhaust flow is controlled for a considerable portion of the midbody for a ratio of 2.36, Fig. 22d. Since the prototype operates between a jet ratio of 2.0 and 2.36, the difference between the flow patterns shown in Figs. 22c and 22e are quite important. The difference between the flow patterns shows the changes which can occur for small variations in flow ratios.

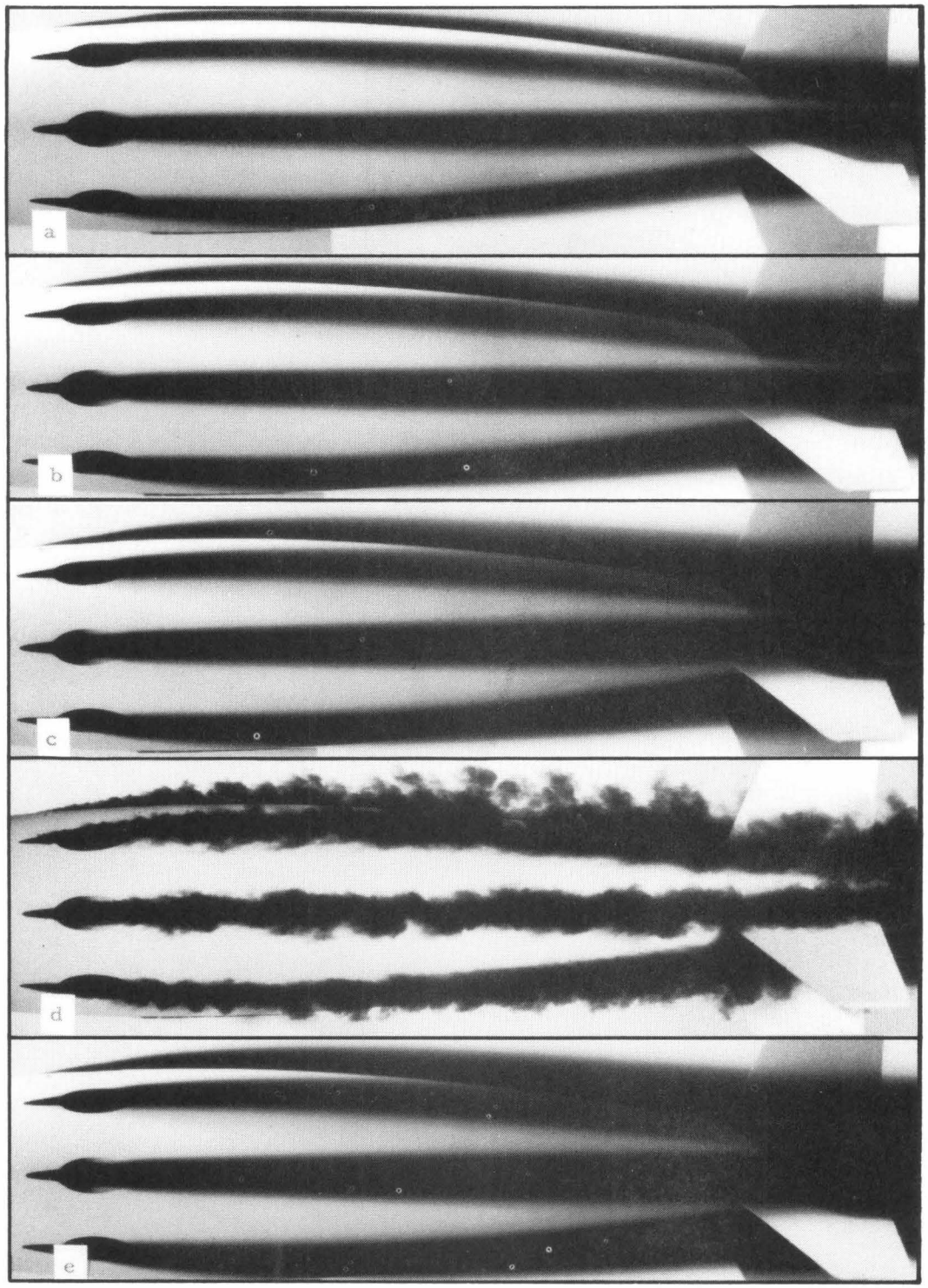

Fig. 21 - Effect of jet velocity ratio on jet flow patterns. Tunnel velocity 30 fps.

a. Jet velocity ratio 1.0
b. Jet velocity ratio 2.0
c. Jet velocity ratio 2.36
d. Jet velocity ratio 2.36 (15 microsecond flash photograph)
e. Jet velocity ratio 2.7

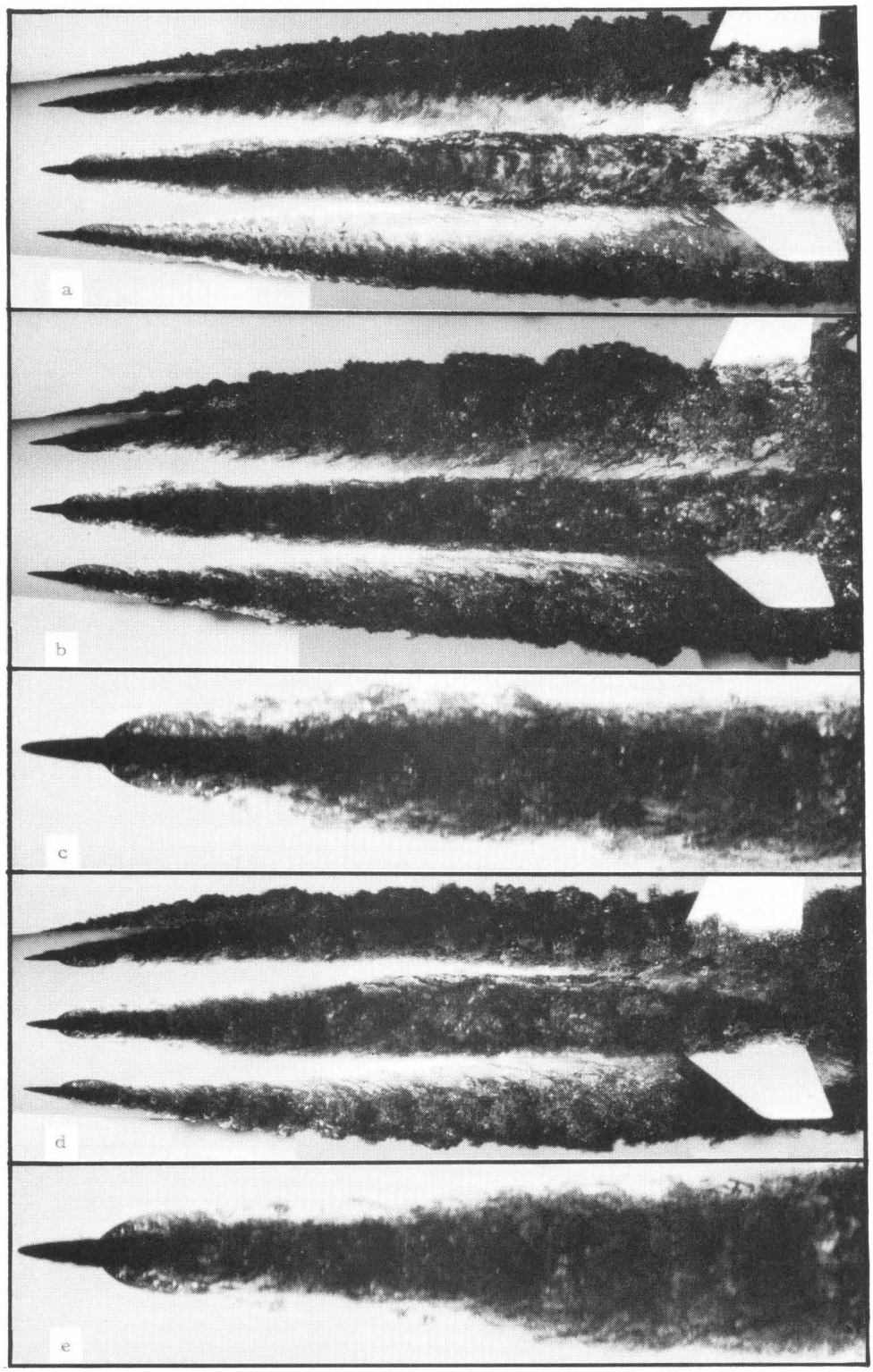

Fig. 22 - Effect of jet velocity ratio on entrainment of exhaust gases.
Exhaust ratio 1.4. Tunnel velocity 30 fps.
(15 microsecond flash duration photographs)
a) Jet ratio 1.0 b) c) Jet ratio 2.0 d) e) Jet ratio 2.6

Figures 18 and 19 show the jet and exhaust flow patterns at a jet ratio of 2.36 for various exhaust velocity ratios.

The surface area which the jet appears to influence was estimated from the photographs shown in Fig. 21. Immediately behind the exhaust port the jet spreads circumferentially so that the jet width is approximately twice the radial extent of the jet, Fig. 23. The jet cross section is considerably distorted from its original circular shape. In this region the jet-affected area is based on the plan-view width of the jet. Near the tail the width and radial extent of the jet are similar. Up to the point where the width is equal to the radial extent, the jet-affected area is based on the jet width. From this point aft, the jet extent is greater than the jet width. The jet becomes distorted in the radial direction. It is assumed that aft of the above mentioned point the jet starts to separate from the body. A triangular area from this point to the tip of the tail is assumed to approximate the jet-affected surface area, Fig. 23.

Appendix IV presents data regarding the flow of exhaust gases only.

II. Pressure Distribution Measurements

A complete pressure survey over the model afterbody for one-third of the circumference was obtained for a variety of flow conditions. Figure 7b shows the averaged afterbody pressure coefficients for jet-to-tunnel velocity ratios of 0 and 2.36. Note the sharp low pressure peaks and the downstream local pressure increases. The effects of jet flow are discussed in the text.

Figure 12 shows the effect of exhaust gas flow on the afterbody pressure coefficients.

These data are considered accurate within a pressure coefficient of ± 0.010.

III. Drag Measurement Data

Afterbody form drag coefficients were calculated from the pressure distribution data. Figure 24a shows the effect of jet flow and Fig. 24b shows the effect of exhaust flow on the calculated afterbody form drag coefficients. The two separate curves for the finned body were obtained by two separate fairing techniques.

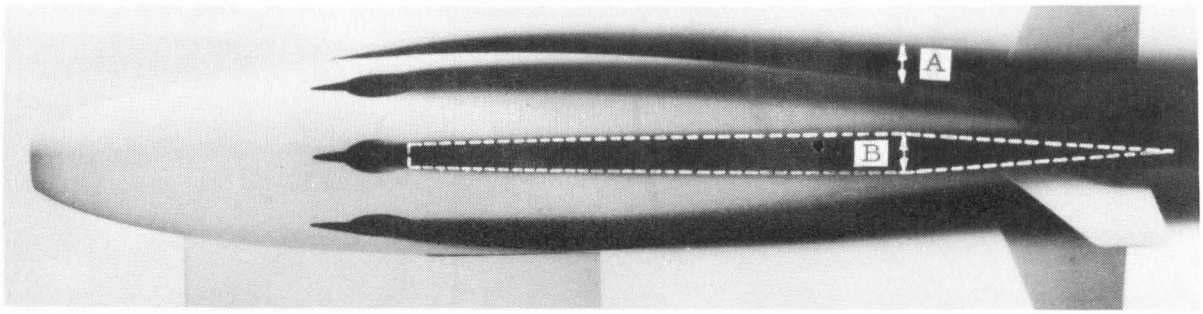

Fig. 23 - Method of estimating the jet affected area. Circumferential width of affected area is assumed equal to width of jet except where the radial extent of the jet (A) exceeds the width (B). From this point the width is assumed to decrease to zero at the end of the body.

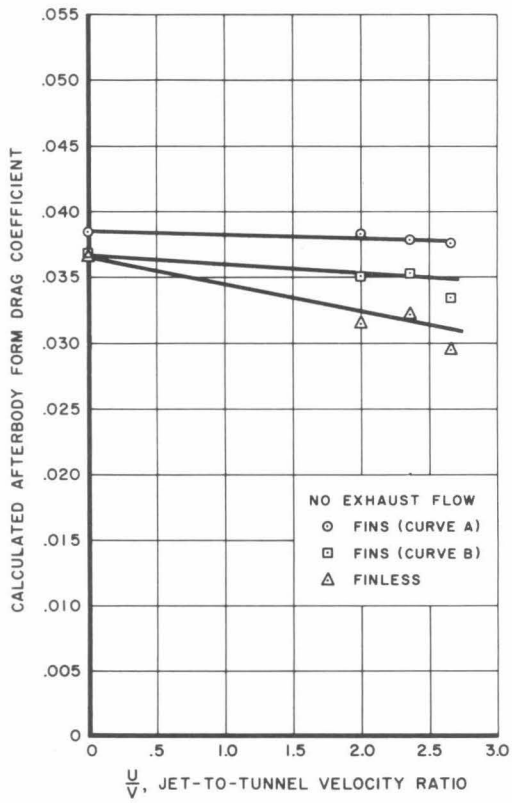

Fig. 24a - Calculated effect of jets on afterbody form drag. Tunnel velocity 30 fps.

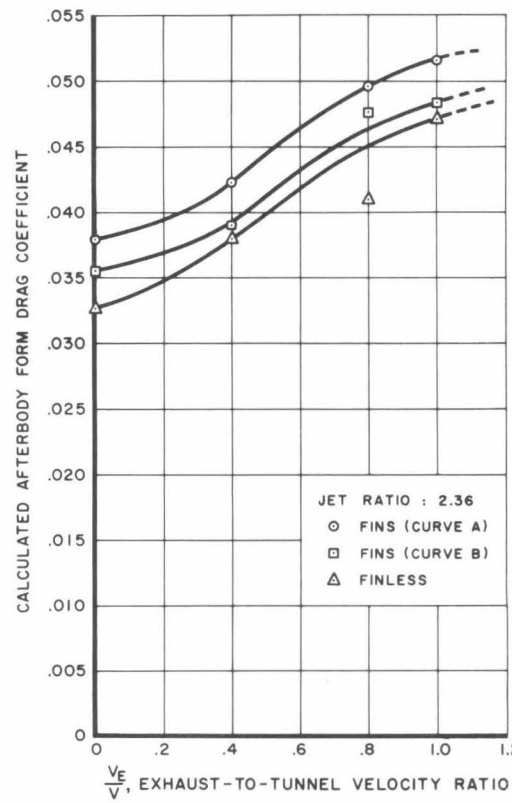

Fig. 24b - Calculated effect of exhausts on afterbody form drag. Tunnel velocity 30 fps.

Figure 25 shows the finless afterbody total drag coefficient as a function of Reynolds number for no jet flow. The calculated total drag is shown for comparison. The two curves are within a drag coefficient of 0.008 of each other for Reynolds numbers greater than 2×10^6. The data for the afterbody with fins is shown in Fig. 26. A thin strip of lacquer paint along the fins was used to stimulate turbulent flow over the fins for the data shown in Fig. 27. The prototype afterbody drag force, based on an extrapolation of the calculated model drag is shown in Table II.

The effect of jets on the afterbody drag coefficients is shown in the text, Fig. 8.

Figure 28 shows the change in afterbody drag coefficient as a function of the exhaust velocity ratio for a tunnel velocity of 25 and 30 fps. The difference between the curves is probably due to the different jet velocities, exhaust velocities, ambient velocities, jet turbulence levels, jet impingement effects and others. Since too little is definitely known of these factors, the quantitative applicability of the data is limited.

IV. Exhaust Gas Flow Only

Figure 29 shows the flow patterns of the simulated exhaust gases for several exhaust velocity ratios with no jet flow. Note the full attached cavities which occur for even the smallest ratios. Major portions of the afterbody are completely enclosed within the gas cavities, obviously greatly increasing the afterbody form drag. Figure 30 shows the effect of the exhaust gas flow (no jet flow) on the afterbody drag coefficient as a function of the exhaust velocity ratio. The change in the total afterbody drag coefficient, Fig. 30, increases rapidly with increased exhaust velocity ratios. The afterbody skin friction drag coefficient is reduced by the decrease in the surface area which contacts the free stream. Thus the increase in form drag coefficient is greater than the increase in total drag coefficient. An approximate calculation for a noncondensable exhaust velocity ratio of 0.6 shows a reduction in the model afterbody friction drag coefficient of 0.025. Since the total increase in afterbody drag coefficient for this exhaust ratio is 0.093, the actual increase in model afterbody form drag coefficient is 0.118. Extrapolating the form drag for the prototype at top speed, results in an increase in drag force of 4025 lbs at a noncondensable exhaust ratio of 0.6 with no jet flow. This

is 136% of the total drag reported in Ref. 1. At the same time the prototype skin friction drag would be reduced 475 lbs. Thus, the net effect of discharging the exhaust gases without the operation of the water jets would be to increase the prototype afterbody drag 3550 lbs. This is 120 percent of the total prototype drag force reported in Ref. 1. From the data presented in the text for combined jet and exhaust flow, the increase in afterbody form drag would be approximately 275 lbs for an exhaust ratio of 0.6 and a jet ratio of 2.36. This is only 9% of the total drag reported in Ref. 1. Thus, the flow of the water jets causes sufficient entrainment of the exhaust gases to greatly reduce the exhaust-induced afterbody drag force.

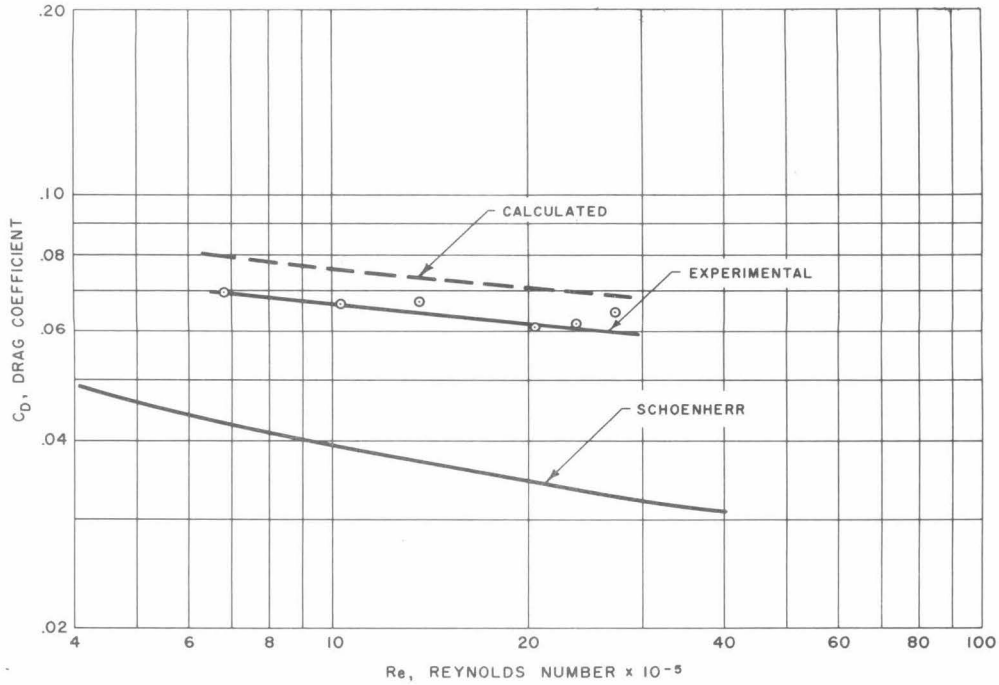

Fig. 25 - Afterbody drag coefficients of finless Model TTV Mk 40 X-1.

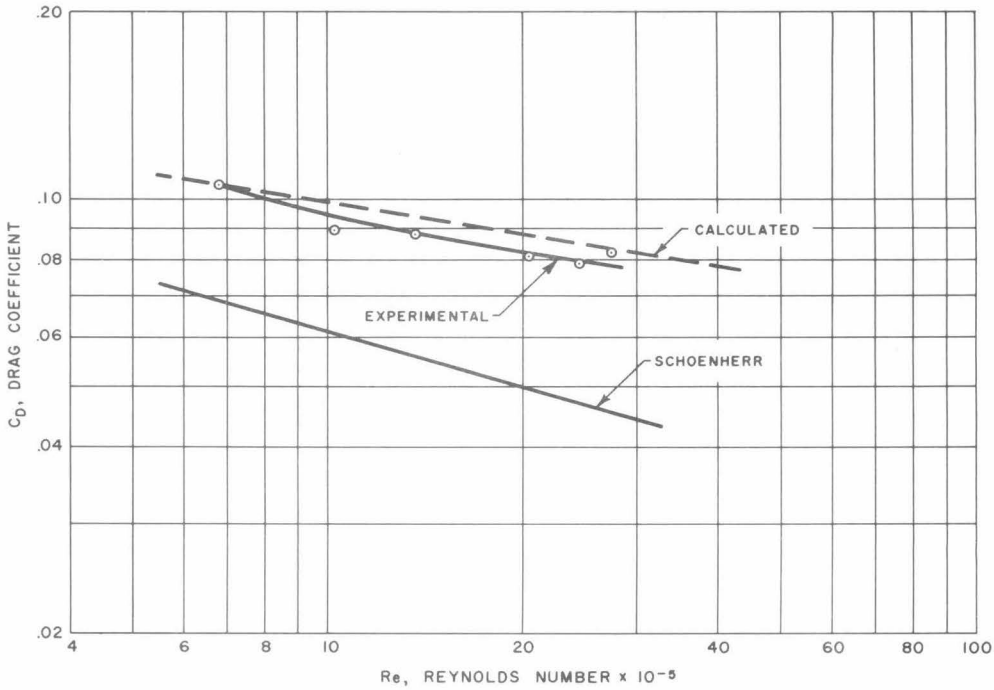

Fig. 26 - Afterbody drag coefficients of Model TTV Mk 40 X-1 with plain fins.

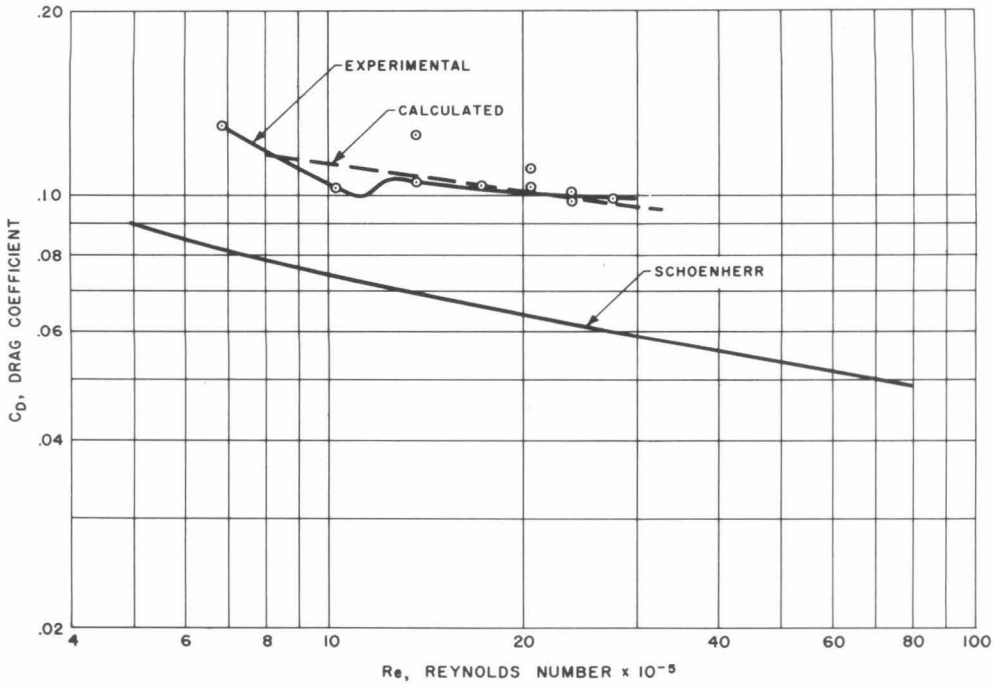

Fig. 27 - Afterbody drag coefficients of Model TTV Mk 40 X-1 with stimulated turbulent flow on the fins.

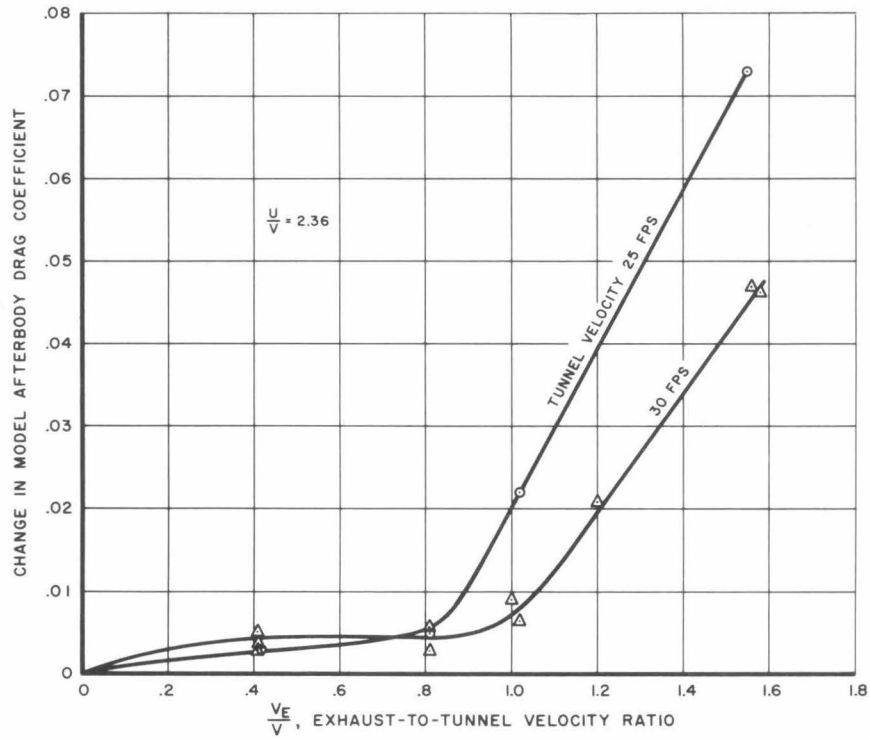

Fig. 28 - Effect of ambient velocity on the afterbody drag coefficient with jet and exhaust flow. Jet velocity ratio 2.36.

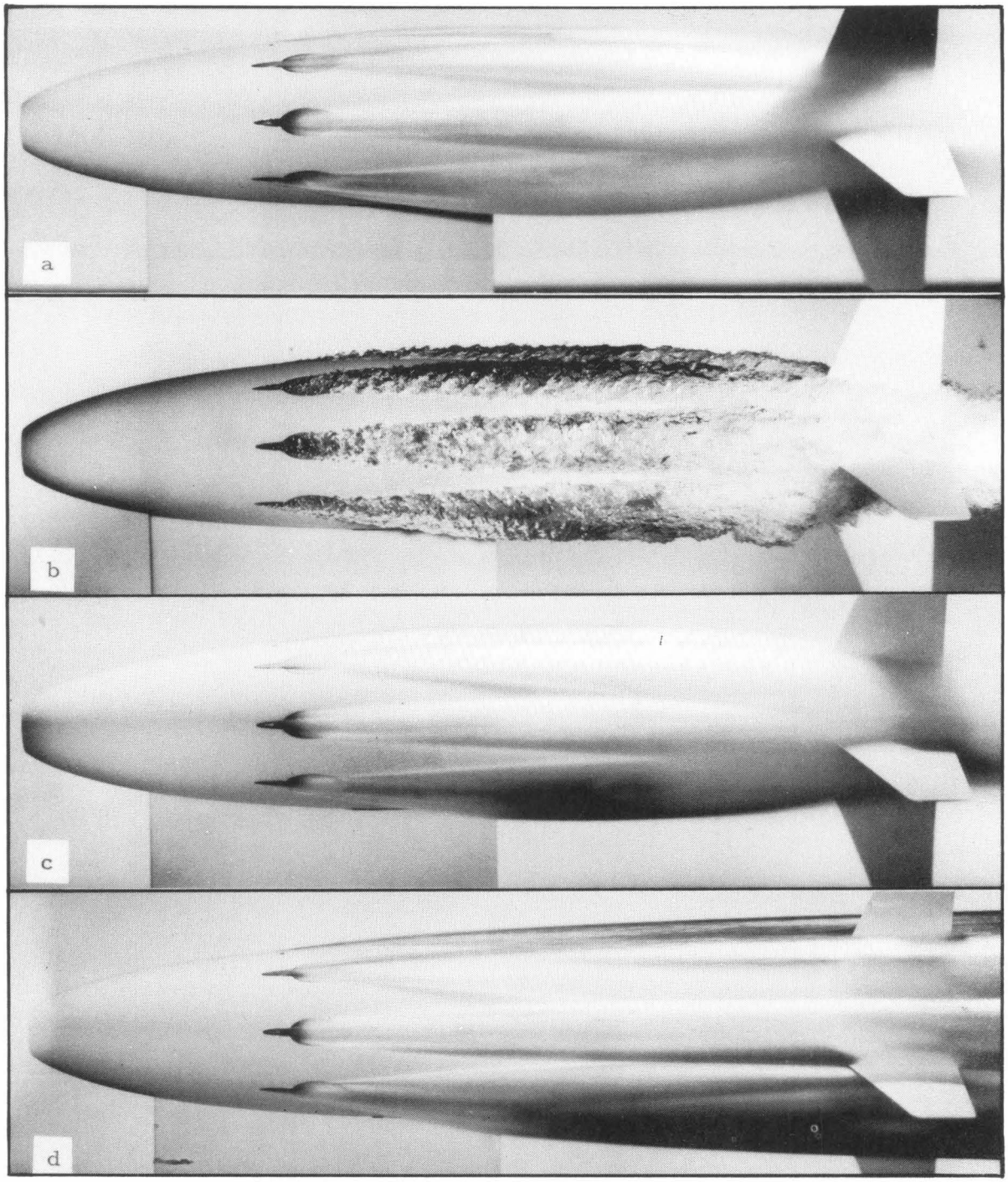

Fig. 29 - Flow pattern of exhaust gases only. Tunnel velocity 30 fps.
a. Exhaust velocity ratio 0.4
b. Exhaust velocity ratio 0.6
(15 microsecond flash photograph)
c. Exhaust velocity ratio 0.6
d. Exhaust velocity ratio 1.0

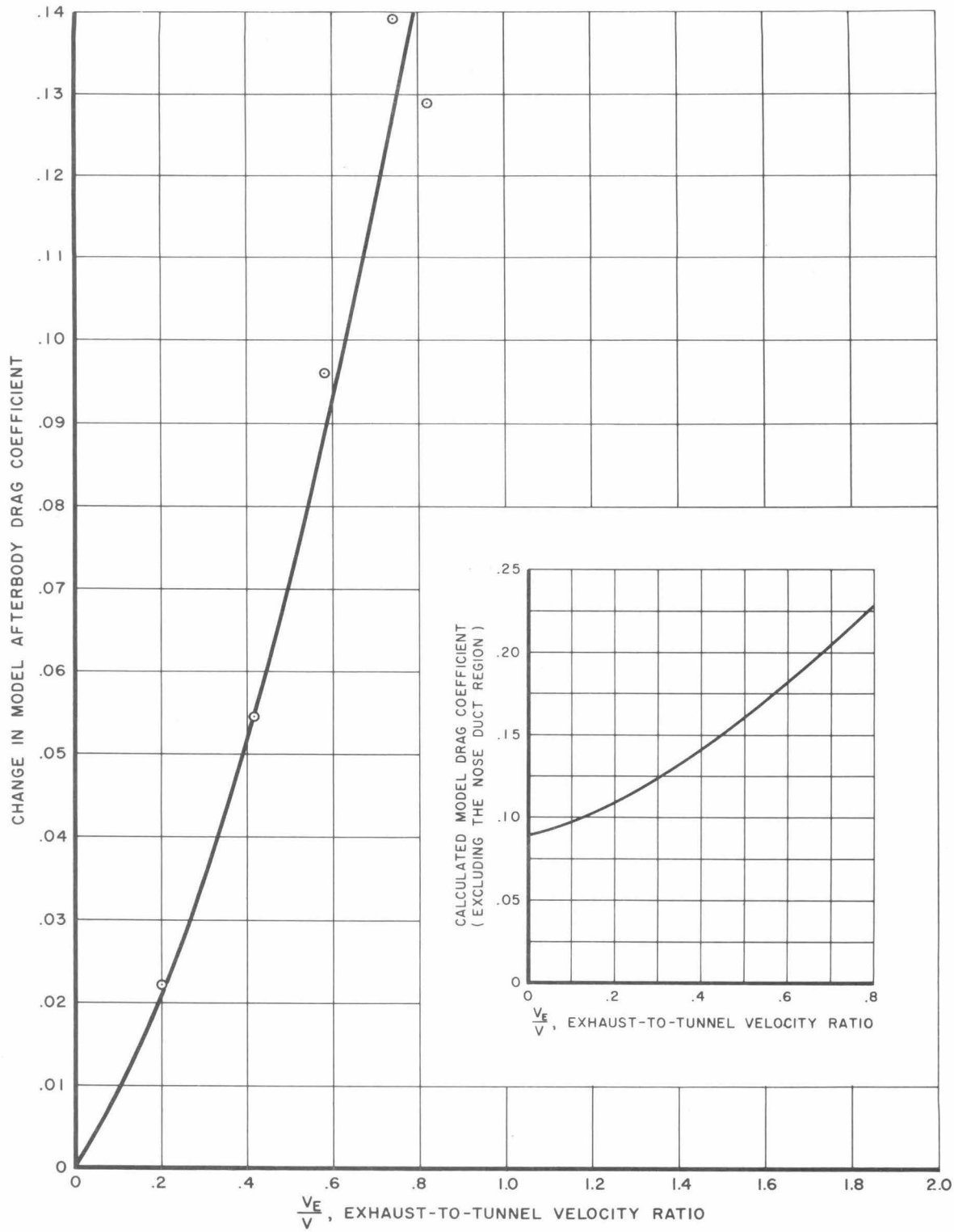

Fig. 30 - Effect of exhaust flow (no water jet flow) on the model afterbody drag coefficient. Tunnel velocity 30 fps.

BIBLIOGRAPHY

1. Brumfield, R.C., "Evaluation of the Technical Program on the High-Speed Torpedo Test Vehicle Mk 40 X-1", Part I, China Lake, California, 5 February 1953 (NAVORD Report 1919, NOTS 643), CONFIDENTIAL.

2. Brumfield, R.C., "Evaluation of the Technical Program on the High-Speed Torpedo Test Vehicle Mk 40 X-1", Part II, China Lake, California, 12 March 1952 (NAVORD Report 1919, NOTS 457), CONFIDENTIAL.

3. Strumpf, A., "Model Study of the Effect of Hydrojet Propulsion System on the Drag of the Proposed Mk 40 Test Vehicle", Experimental Towing Tank, Stevens Institute of Technology, Report No. 396, April 1950, CONFIDENTIAL.

4. Waid, R.L., "A Scale Model Investigation of the Effects of Jet Configuration on Skin Friction for the Mk 40 Torpedo", Hydrodynamics Laboratory, California Institute of Technology, Report No. E-12.6, September 1952, CONFIDENTIAL.

5. Lyon, H.M., "Effect of Turbulence on Drag of Airship Models", Air Ministry, Air Research Committee, Reports and Memorandum No. 1511, August 1932.

6. Becker, J.V., "Wind Tunnel Tests of Air Inlet and Outlet Openings on a Streamline Body", NACA ACR (WR L-300) November 1940.

7. McGraw, J.T., Kermeen, R.W., Jackson, V.G., "The Effect of Jets on the Drag and Cavitation Characteristics of a Two-Dimensional Body", Hydrodynamics Laboratory, California Institute of Technology, Memorandum Report No. EM-12, July 2, 1951, CONFIDENTIAL.

8. Gertler, M., "The Prediction of the Effective Horsepower of Ships by Methods in Use at the David Taylor Model Basin", David Taylor Model Basin Report 576, September 1947.

9. Rouse, H., McNown, J.S., "Cavitation and Pressure Distribution, Head Forms at Zero Angle of Yaw", Iowa Institute of Hydraulic Research, State University of Iowa, Bulletin 32, 1948.

10. Kermeen, R.W., "Cavitation Tests on Models of NOTS Torpedo Test Vehicles and a Cable Shoe for the Underwater Cable Range", Hydrodynamics Laboratory, California Institute of Technology, Report No. E-44, August 1953, CONFIDENTIAL.

Department of the Navy
Bureau of Ordnance
Contract NOrd 9612

DISTRIBUTION LIST

Copy No.	
1	Chief, Bureau of Ordnance Navy Department (Attn:Code Re6a) Washington 25, D.C.
2	Chief, Bureau of Ordnance Navy Department (Attn:Code Re3d) Washington 25, D.C.
3-4	Chief, Bureau of Ordnance Navy Department (Attn:Code Ad3) Washington 25, D.C.
5-7	Chief, Bureau of Aeronautics Navy Department (Attn:Code De3) Washington 25, D.C.
8-12	Chief, Bureau of Ships Navy Department Washington 25, D.C.
13-15	Chief, Office of Naval Research Navy Department (Attn:Code 438) Washington 25, D.C.
16	Director, ONR Branch Office 1030 East Green Street Pasadena 1, California
17-18	Director, David Taylor Model Basin Washington 7, D.C.
19-20	Commanding Officer U.S.N. Underwater Ord. Station Newport, R.I.
21-22	Commander, Naval Ordnance Lab. White Oak Silver Spring 19, Maryland
23-25	Officer-in-Charge, Pasadena Annex Naval Ordnance Test Station 3202 E. Foothill Blvd. Pasadena, California Attn: Pasadena Annex vLibrary (Code P5507)
26	Director, Experimental Towing Tank, Stevens Inst. Technology via: Bureau of Aeron. Rep. c/o Bendix Aviation Corp. Eclipse-Pioneer Division Teterboro, New Jersey
27	Director, Ordnance Research Lab. Pennsylvania State College State College, Pennsylvania
28	Alden Hydraulic Laboratory Worcester Polytechnic Institute via: Inspector of Naval Material 495 Summer Street Boston 10, Mass.
29	Inspector of Naval Material Development Contract Section 1206 S. Santee Street Los Angeles 15, California
30-31	Librarian, U.S. Naval Post-graduate School Monterey, California
32-33	Director, U.S. Naval Electronics Laboratory Point Loma, San Diego, Calif.
34-43	British Joint Services Mission, Navy Staff via: Chief, Bureau of Ordnance Navy Dept. (Attn: Code Ad8) Washington 25, D.C.
44	Executive Secretary Research and Development Board National Defense Building Washington, D.C.
45	Phillip Eisenberg Office of Naval Research Mechanics Branch Washington 25, D.C.
46	Commander, Submarine Development Group TWO Box 70 U.S. Naval Submarine Base New London, Conn.
47	Dr. F. C. Lindvall 200 Throop California Institute of Technology Pasadena, California